Microphysiological stroke model for systematic evaluation of neurorestorative potential of stem cell therapy

Wonjae Lee (lee.wonj@gmail.com)
Stanford University https://orcid.org/0000-0003-1524-2259

Zhonlin Lyu
Stanford University

Jon Park
Stanford University

Kwang-Min Kim
Stanford University

Hye-jin Jin
Stanford University

Haodi Wu
Stanford University

Jayakumar Rajadas
Stanford University

Deok-Ho Kim
Johns Hopkins University

Gary Steinberg
Stanford Medicine

Article

Keywords: Ischemic Stroke, Experimental Platform, Neurovascular Unit, Microfluidic Chip, Blood-brain Barrier, Endogenous Recovery, Synaptic Activity Recovery

Posted Date: March 19th, 2021

DOI: https://doi.org/10.21203/rs.3.rs-96280/v1

Title: Microphysiological stroke model for systematic evaluation of neurorestorative potential of stem cell therapy

Authors: Zhonglin Lyu[1,†], Jon Park[1,†], Kwang-Min Kim[1,2,†], Hye-Jin Jin[1], Haodi Wu[2], Jayakumar Rajadas[2], Deok-Ho Kim[4,5], Gary K. Steinberg[1,3], Wonjae Lee[1,3,*]

Affiliations:
[1] Department of Neurosurgery, Stanford University School of Medicine, Stanford, CA, USA.
[2] Department of Medicine, Stanford University School of Medicine, Stanford, CA, USA.
[3] Stanford Stroke Center, Stanford University School of Medicine, Stanford, CA, USA.
[4] Departments of Biomedical Engineering, Johns Hopkins University School of Medicine, Baltimore, MD, U.S.A.
[5] Departments of Medicine, Johns Hopkins University School of Medicine, Baltimore, MD, U.S.A.
* Corresponding author, Wonjae Lee, wonjae.lee@stanford.edu
[†] Authors equally contributed.

ABSTRACT

Stem cell therapy is emerging as a promising treatment option to restore a neurological function after ischemic stroke. Despite the growing number of candidate stem cell types, each with unique characteristics, there is a lack of experimental platform to systematically evaluate their neurorestorative potential. When stem cells are transplanted into ischemic brain, the therapeutic efficacy primarily depends on the response of the neurovascular unit (NVU) to these extraneous cells. In this work, we developed an ischemic stroke microphysiological system (MPS) with a functional NVU on a microfluidic chip. Our new chip design facilitated the incorporated cells to form a functional blood-brain barrier (BBB) and restore their *in* vivo-like behaviors in both healthy and ischemic conditions. We utilized this MPS to track the transplanted stem cells and characterize their neurorestorative behaviors reflected in gene expression levels. Each type of stem cells showed unique neurorestorative effects, primarily through supporting the endogenous recovery, rather than through direct cell replacement. And the recovery of synaptic activities, critical for neurological function, was more tightly correlated with the recovery of the structural and functional integrity in NVU, rather than with the regeneration of neurons itself.

INTRODUCTION

Ischemic stroke is caused by an inadequate supply of blood to the brain and leads to deficits in neurologic functions[1]. The stroke involves a series of spatial and temporal events, such as inflammatory and immune responses, cell death and differentiation, hypoxia, vascular damage, and altered cerebral microenvironment[1]. Stem cell therapy has been highlighted as an emerging paradigm for stroke treatment, with supports from experimental animal studies as well as clinical pilot studies[2]. The clinical outcomes of stem cell therapies depend on a variety of factors, including the route, dosage, and timing of administration, but the most critical factor appears to be the type of stem cells[2]. Each type of stem cells has unique traits and distinct regenerative potential[2], and yet there is a lack of reliable stroke model to systematically compare the efficacy across the broad range of candidate cell types and to investigate the underlying mechanism of stem cell therapeutics[3]. This poses a major challenge in utilizing and advancing stem cell therapies.

The most widely used experimental platform for developing and examining stem cell therapeutics is the murine-based animal models and several approaches have shown some enhanced neuroprotective effects in animal studies[4]. While outcomes from early phase cellular transplant clinical trials look promising, they do not always replicate the results from animal stroke models[5]. This might be due to the intrinsic differences between animal models and the human disease in terms of anatomy and physiology, the pathophysiological responses to injury, or the injury mechanism[6]. The animal models also have the inherent limitations in time- and cost-efficiency to be an ideal platform for characterizing the therapeutic potentials of multiple stem cell types on the entire cascade of pathological events induced by the stroke.

The neurovascular unit (NVU) plays critical roles in the stroke progression as well as the recovery process[7]. NVU consists of brain microvascular endothelial cells (BMEC) and their neighboring neural cells, i.e. neurons and multiple types of glia cells[7]. These constituent cells in NVU work in concert with one another and create a tight blood-brain barrier (BBB) that regulates the molecular transport into and out of the brain parenchyma to maintain the homeostasis of the neural microenvironment as well as the brain functions[7]. NVU not only mediates the drug delivery and infiltration of the transplanted stem cells into the ischemically damaged brain parenchyma, but also engages in the fate determination of neural stem cells during post-stroke neuroregeneration[7].

Due to the clinical significance of BBB in drug delivery to brain parenchyma, there have been continuous efforts to develop *in vitro* BBB models. Major approaches in the past include BBB models with Transwell, a cone and plate viscometer, and hollow fibers[8]. More recently there have been some notable advances in constructing functional BBB on a microfluidic chip[8-12]. However, most of these approaches have limitations to be directly applicable to establishing the complex 3D tissue environment associated with the pathophysiological conditions of ischemic stroke and the recovery process by transplanted stem cells.

In this study, we developed a stroke microphysiological system to examine the neurorestorative capacity of stem cell therapy. Our stroke model uses human-derived cells and has the *in vivo*-like 3D microenvironment recapitulating the natural interaction between the transplanted stem cells and the host cells of the NVU. Our model served as a reliable screening platform to systematically analyze the neurorestorative behaviors of various stem cell types currently tested in clinics for stroke treatment.

RESULTS

Chip design for the reconstruction of functional BBB

The key advantage of *in vitro* model is the capacity of the real-time monitoring of the cell behaviors. In order to efficiently observe the hierarchical cell behaviors during the disease progression and recovery, we applied a widely used design of multi-channel microfluidic chip[13] in which different types of cells are positioned side-by-side on the same focal plane of traditional optical microscopes (**Fig. 1A**). The overall process to prepare the samples is described in **Table S1** in Supplementary Information (S.I.). Our microfluidic chip has three channels; the 'blood-side' channel through which the bloodstream is simulated, the 'brain' channel in which the neural cells form a native 3D structure in a hydrogel matrix, and the 'cerebrospinal fluid (CSF)-side' channel which provides an additional access to the neural cells in the 'brain' channel (**Fig. 1A i - iii**). For the hydrogel matrix, we used a soluble form of basement membrane purified from Engelbreth-Holm-Swarm (EHS) tumor (Cultrex™, Trevigen) with major components of laminin, collagen IV, entactin, fibronectin, entactin, and heparan sulfate proteoglycans. The basement membrane derived from EHS tumor has an elastic modulus of around 0.5 kPa[14], within the range of the physiological stiffness of brain tissues[15], and supports the neuronal differentiation of NPC[16] as well as neuronal survival and functions[17]. In the initial chip design, we had adopted an approach[13] where each microfluidic channel was separated by micro-poles to generate the surface tension necessary to confine the liquid hydrogel prepolymer within the designated channel (**Fig. S1** in S.I.). An endothelium was to be formed on the side wall of the hydrogel in the 'brain' channel, perpendicular to the x-y plane of the entire structure. However, we found that these micro-poles interfered with the endothelial cells and kept them from forming a continuous and intact endothelium, causing physical defects (**Fig. S1** in S.I.**)**. These defects could be a major pitfall in assessing the actual efficacy of the stem cell therapeutics using our model, because they would serve as an artificially easy shortcut for the stem cells or bioactive substances in the bloodstream to reach the ischemically damaged brain.

We thus conceived a new chip design without any micro-poles but still with the real-time monitoring capacity in the same microscopic focal planes. With the new design, the height of the middle 'brain' channel was lowered to generate the surface tension between the top and the bottom surfaces (**Fig. 1A i-iii**) and to stably hold the liquid hydrogel prepolymer in the 'brain' channel (**Fig. 1A iv**). As expected, a well-defined boundary was formed between the 'blood-side' and 'brain' channels in the new chip (**Fig. 1A v-vi**). The reconstructed endothelium successfully prevented free diffusion of a fluorescent probe (FITC-dextran, 4 k Da) across itself (**Fig. 1A vii**). The probe size of 4k Da is useful to evaluate the BBB functionality because most pathogens, such as viruses and bacteria, are larger than 4k Da and the native BBB prevents these pathogens from entering the brain[8]. Single layer of the confocal microscopic images showed the continuous and physically intact endothelial barrier (**Fig. 1A viii**) in contrast to the one in the previous chip design with micro-poles (**Fig. S1** in S.I.). Our new chip design is devoid of micrometer-scaled features, eliminating the need for the soft lithography process in chip production, and enables us to utilize a 3D printer (**Fig. S2** in S.I).

We found that both astrocytes and pericytes were required for the endothelial cells to form the physically intact endothelium on the side wall of the 'brain' channel (**Fig. 1A ix**). Before the endothelium formation, there was a small population of astrocytes in the 'blood-side' channel migrating from the 'brain' channel (0.9 ± 0.3 (s.d.) % of the totally incorporated astrocytes, n=3, **Fig. S3** in S.I.). These migrated astrocytes, together with pericytes, supported BMEC to maintain the normal morphology of a smooth rounded shape throughout the 'blood-side' channel (**Fig. S4** in S.I.), just like the morphology of BMEC when co-cultured with both astrocytes and pericytes in 2D culture[18]. The astrocytes and pericytes in the 'blood-side' channel settled beneath the layer of the endothelial cells at the bottom, as the BMEC

connected to each other, maturing to form an endothelium (**Fig. S3** in S.I.). It might be due to the angiogenic process in which endothelial cell-to-cell junctions strengthen the connection between the neighboring endothelial cells[19].

We examined the endothelial tightness under different conditions, depending on the cell composition and the presence of flow, by calculating the apparent permeability coefficients (**Fig. 1A x**). In the presence of astrocytes and pericytes, the endothelium became significantly tighter to hinder the diffusion of the probe, FITC-dextran (**Fig. 1A x**). Further significant reduction in the permeability was observed after the flow of culture media was introduced (**Fig. 1A x**). This tightening of the endothelium in the presence of flow is in line with the reports of enhanced paracellular connectivity in BBB by proper mechanical stimuli[8]. The permeability coefficients are comparable to those of other *in vitro* and *in vivo* BBB models previously reported [20]. The reconstructed BBB also showed the expected size-selective permeability as in functional BBB[21]; the smaller the probe size, the better the diffusion across the BBB (**Fig. 1A x**). Another standard measure to assess the BBB tightness is Trans-Endothelial Electrical Resistance (TEER) [22]. TEER measurement is a simple, label-free and non-invasive method to quantify the barrier integrity. There is a broad range of TEER values reported for microfluidic BBB models, from a few hundred [12,23-25] to thousands[26,27] of $\Omega \cdot cm^2$, while their permeability coefficients are within a relatively narrow range of around 1×10^{-6} cm/s for 4k Da FITC-Dextran. This might be because the TEER values are largely dependent on the method of measurement and experimental procedures[28]. Alternative currents (AC) are widely used for TEER measurement because direct currents (DC) can damage cells [22]. Due to the small surface area of the BBB in our chip, however, the resistance across the BBB was expected to reach several mega-ohms, beyond a measurable range of AC TEER meters commercially available. We therefore used a DC meter and the measured TEER value of the BBB in our chips was 370 ± 20 (s.d.) $\Omega \cdot cm^2$ under the flow (**Fig. S5** in S.I.). The TEER value measured in our chip is lower than those reported in some of the microfluidic BBB models[26,27], but showed meaningful differences between conditions (**Fig. S5** in S.I.).

Once we confirmed the physical intactness of the endothelium, we examined the functional characteristics of the reconstructed endothelium as a bio-chemically intact barrier. One of the important functions of the cerebral endothelium *in vivo* is to isolate the neural cells in the brain parenchyma from any pro-inflammatory substances in the bloodstream[7]. To maintain the original phenotype of the cells in each channel of our chip, we deployed two different types of media: serum-containing endothelial media in the 'blood-side' channel and serum-free glial cell media in the 'CSF-side' channel (**Fig. 1B i**). The reason for this setup is that the endothelial cells require serum to maintain their original phenotype *in vitro,* whereas the glia cells show pro-inflammatory behaviors in the serum-containing culture medium[29]. Serum, extracted from the whole blood, is an undefined mixture of proteins, hormones, minerals, growth factors, and lipids. The reconstructed BBB thus needs to prevent the entry of any pro-inflammatory substances from the serum in the 'blood-side' channel. In the samples without BBB, the microglia, a resident immune cell type in the brain, showed pro-inflammatory behaviors as expected (**Fig. 1B ii**) because they were directly exposed to the serum. In contrast, in the samples with the reconstructed BBB, the microglia did not show such pro-inflammatory behaviors (**Fig. 1B iii & iv**), confirming the BBB in our chip as a bio-chemically intact barrier, similar to the native BBB[29].

To be a clinically relevant platform for stem cell therapy, the BBB on our chip should also exhibit distinct responses based on the traits of the invading cells. The neurorestorative efficacy of each stem cell type may depend on their capacity to infiltrate across the tight BBB and reach the lesion site, and yet little

is known about the native BBB responses to the candidate types of stem cells in therapy. Therefore, as a valid measure to show the cell-selective responsivity of the BBB, we propose to utilize the well-established metastatic behaviors of the two human breast cancer cell lines, MB-231 and its brain metastatic derivative population, MB-231Br. MB-231Br infiltrates specifically across the BBB and exhibits much stronger metastatic tendency than MB-231 in an animal model[30]. The reconstructed BBB in our stroke model showed the expected cell-specific responses to these two types of invading cancer cells (**Fig. 1C**), confirming the *in vivo*-like functionality of our model and verifying its sensitivity to the traits of the invading cells.

Establishing the ischemia

After confirming the formation of a functional BBB in our chip, we established an ischemic condition. There are two major zones of ischemic injury: the *core infarct zone* and the *ischemic penumbra*, also called as *peri-infarct rim*[31]. The *core infarct zone* is characterized by no blood supply and severe necrosis of neural cells, and is considered irreversibly injured[31]. In contrast, the *ischemic penumbra*, the rim surrounding the irreversibly damaged core, has just enough blood supply for the cells to survive but not enough to communicate and function properly[31]. This *peri-infarct rim* has been considered as a therapeutic target for post-stroke recovery[32,33]. We thus targeted to establish an ischemic condition recapitulating this *peri-infarct zone*, sufficiently damaging the cells and yet minimizing cell death.

The optimized ischemic condition in our system was 2% O_2 with depletion of serum and glucose for 24 hours, in the absence of flow[34]. Our ischemic condition sustained the cell viability (**Fig. 2A i - iii**), while inducing detectable cytotoxicity (**Fig. 2A iv**) measured by the amount of the extracellular lactate dehydrogenase (LDH) released through the damaged cell membranes. We also observed that hypoxia-inducible factor-1α (HIF-1α), usually found in the cytoplasm of the cells under normoxic condition (**Fig. 2A v - vi**), translocated to the nucleus (**Fig. 2A vii - viii**), as observed in the ischemic brain *in vivo* [35]. According to the gene expression alteration pattern in our chip (**Fig. 2B**), the ischemic insult upregulated the genes in both the apoptotic and the antiapoptotic signaling cascades (***Apoptosis*** group), just as reported in animal ischemic stroke model[36]. Oxidation-reduction reaction (***Redox*** group) was also upregulated, implying the cells protected themselves against the elevated intracellular levels of reactive oxygen species in ischemia[37]. The upregulation of the neurotrophic and angiogenic factors (***Trophic factors*** group) suggest the attempts of the ischemically damaged cells to repair and remodel themselves[38]. The cells also exhibited typical neuroinflammatory responses against ischemic stroke[39] as shown in the upregulated gene expressions of ***Pro-inflammatory cytokines*** and ***Integrin*** groups. The downregulated expression of extracellular matrix proteins (***ECM proteins*** group), together with the enhanced activities of matrix metalloproteinases (***MMP*** group) and the decreased interaction between the cells and ECM (***Cell adhesion*** group) imply that the ischemic insult led to the impairment of tissue integrity as well as the subsequent tissue remodeling process. Overall, these gene expression patterns collectively indicate that our ischemic condition successfully induced inflammation and deterioration in tissue integrity as expected and also accompanied endogenous neuroprotection and tissue remodeling, as reported in many other *in vivo* stroke models[38].

Verifying the NVU behaviors

To verify the functionality of the reconstructed NVU, we examined individual cell behaviors at various levels both under healthy and ischemic conditions. At gene level, we measured the expression alteration of the genes associated with a series of post-stroke pathological conditions and categorized them based on their functional characteristics. Since most of the genes are not cell-specific and involved in

203 multiple cellular processes, this grouping is solely for the purpose of outlining the overall pattern of the
204 responses across the cell population in our experiments. More detailed information on individual genes is
205 presented in **Table S2** in S.I.

206 ***Neurons*** are the primary component of the central nervous system and play critical roles in
207 neurological functions. Considering the short lifespan and limited expansion capacity of the primary
208 human neurons *in vitro*, we used the human iPSC (induced pluripotent stem cell)-derived neural progenitor
209 cells (NPC) in our stroke model and optimized the culture conditions of the chip for their neuronal
210 differentiation. The differentiated NPC exhibited the neuronal morphology of a cell body and branches of
211 axons and dendrites (**Fig. 3A i**), and expressed mature neuron markers such as microtubule-associated
212 protein 2 (MAP-2) and Synapsin I and II (SYN), a family of proteins regulating neurotransmitter release
213 at synapses (**Fig. 3A ii**). They also maintained proximity with the astrocytes in our chip (**Fig. 3A iii**).
214 Under ischemic condition, they showed dendritic beading or fragmentation (**Fig. 3A v**), a typical
215 morphology of degenerating neurons[40], compared to the smooth and clear dendritic morphology observed
216 in normoxia (**Fig. 3A i**). They were also stained by a neuronal degeneration marker Fluoro-Jade stain (**Fig.
217 3A iv** vs. **vi**), consistent with the reports from *in vivo* ischemic stroke models[41].

218 The gene expression alteration by the ischemia (**Fig. 3A vii)** shows that the endogenous repair
219 (***Trophic factors*** group **Fig. 2B**) led to the upregulation of the gene groups involved in ***Neurite*** formation
220 and ***Synaptogenesis***, but it was accompanied by downregulation of genes related to ***Synaptic plasticity***.
221 We also observed the excessive stimulation of an excitatory neurotransmitter, glutamate (***Glutamate***
222 group), and at the same time the decreased activity of an inhibitory neurotransmitter, Gamma-
223 Aminobutyric acid (GABA) (***GABA*** group; *ABAT* and *GABRB1* are encoded in an enzyme for GABA
224 catabolism[42] and in one of the GABA receptors[43], respectively). These expression patterns imply the
225 disrupted balance between neuronal excitation and inhibition in the ischemic condition, potentially leading
226 to the excitotoxicity typically observed in ischemic stroke[44].

227 We further examined how the ischemic condition was reflected in the cytosolic calcium (Ca^{2+})
228 oscillation pattern in the differentiated NPC in our chip. The cytosolic Ca^{2+} imaging provides an indirect
229 but accurate measure of the action potential generation in individual neurons [45], and represents various
230 neuronal functions ranging from synaptic activity to cell-cell communication, adhesion,
231 neurodegeneration and apoptosis[46]. The cytosolic Ca^{2+} images show that the differentiated NPC exhibited
232 the typical four patterns of cytosolic Ca^{2+} signals[45]: oscillatory (repeated brief increase in free Ca^{2+}),
233 transient (brief elevation due to Ca^{2+} influx through membrane calcium channels), sustained (sustained
234 increase in Ca^{2+} level by both external and internal stores), or unnoticeable signals (**Fig. 3A viii** & **ix**). The
235 ischemic insult decreased the ratio of cells showing the unnoticeable Ca^{2+} signals, while increasing the
236 ratio of cells showing both transient and sustained signals (**Fig. 3A x** & **xi**). The accumulated Ca^{2+} level
237 in the cytoplasm is thought to lead to neuronal death in animal stroke models[44]. Analysis on the oscillatory
238 signal alteration by ischemia reveals insignificant changes in the amplitude but significant increase in
239 frequency of the oscillation (**Fig. 3A xii** & **xiii**). Since the increased frequency indicates the increased
240 Ca^{2+} influx into the cells [47], these data show that the excitotoxicity due to the excessive release of glutamine
241 (***Neurotransimitters*** group in **Fig. 3A vii**) triggered the excessive influx of Ca^{2+} (**Fig. 3A xi** & **xiii**), which
242 leads to neurodegeneration[48].

243 ***Brain Microvascular Endothelial Cells*** (BMEC) are the primary cellular component of the
244 cerebral vasculature, BBB. Human primary BMEC were used throughout this study. BMEC have a high
245 mitochondrial density, lack of fenestrations, low pinocytic activity, and high density of adherent and tight

junctions compared to the endothelial cells found in other tissues[23,46]. The tight junctions determine the paracellular tightness of the endothelial cells and the permeability across BBB[8]. Zonula occludens-1 (ZO-1) is a dominant junctional adaptor protein, regulating other junctional components, cell-cell tension, angiogenesis, and BBB formation[50]. The flow through 'blood-side' channel increased the expression of ZO-1 and caused the shape of the cell body to elongate along the direction of the simulated bloodstream (**Fig. 3B i-iv**). The upregulated ZO-1 expression in the samples with flow led to the upregulated expression of other junctional proteins, VE-cadherin and Claudin-5 (**Fig. S6** in S.I.). The ZO-1 expression of the ischemic samples significantly decreased compared to the samples in normoxia with the flow, but was statistically comparable to the normoxic samples without the flow (**Fig. 3B v** & **vi**). Importantly, the expression of ZO-1, mainly localized on the cell membrane under normoxia conditions (**Fig. 3B iii** & **vii**), spread throughout the cell body under ischemic conditions (**Fig. 3B v** & **vii**). This dispersed spatial distribution of ZO-1 in the ischemic samples led to the increased permeability of fluorescence probe (4k Da FITC-dextran, **Fig. 3B viii**), representing the reduced paracellular tightness under ischemia[51]. These results suggest that the paracellular tightness among the endothelial cells is affected more significantly by the extent of tight junction localization on the cell membrane, rather than the overall level of their expression. The BMEC in the ischemic samples significantly increased the expression of the vascular endothelial growth factor (VEGF), one of the angiogenic factors (**Fig. 3B v** & **ix**), suggesting the post-stroke vascular reorganization took place in our model, as observed in an animal stroke model[52]. At the gene level (**Fig. 3B x**), the ischemic insult decreased the endothelial paracellular connectivity (***EC-EC junctions*** group), but upregulated the genes involved in ***Vasoconstriction*** and ***Adhesion molecules for recruiting immune cells***, as observed in animal stroke models[53,54].

BMEC behaviors have been well documented in various experimental conditions. In a mono-culture of human BMEC, the shear stress induced by the flow did not significantly affect the expression of the tight junction proteins or their morphology[55]. On the other hand, the flow condition in a mono-culture of bovine BMEC led to the upregulation of tight junction proteins and the morphological alignment along the flow direction[56]. In another *in vitro* work[18], rat BMEC required the appropriate interactions with both the astrocytes and the pericytes to show their original pattern of tight junction localization around the cell membrane, as we observed in our model (**Fig. S4** in S.I.). Taken together, these results suggest that in order for human BMEC to exhibit *in vivo*-like behaviors, they need some of the key components of the original BBB microenvironment: the mechanical stimuli by the blood flow and the heterocellular network in NVU. Our stroke model provides both of these essential microenvironment features, allowing for *in vivo*-like behaviors of human BMEC.

Pericytes are mural cells of the microvasculature, and regulate BBB permeability, angiogenesis, clearance, cerebral blood flow, neuroinflammation and stem cell activity[57]. We used human primary brain vascular pericytes throughout this study. **Figure 3C i** & **ii** show that the pericytes in our chip expressed platelet derived growth factor receptor beta (PDGFRβ), one of the pericyte specific makers[58], and positioned themselves between the mature endothelium and the side wall of the 'brain' channel. More detailed data on pericytes distribution are presented in **Figure S3** in S.I. The pericytes were activated in response to the ischemic injury (***Pericyte markers*** groups in **Fig. 3C iii**), contributing to vascular inflammation[57]. The interaction of pericytes with endothelial cells, crucial for the vascular stability under normal condition[59], was downregulated (***PC-EC interaction*** group).

Astrocytes are the dominant glial cell type in the brain and play many mediating roles in the heterocellular interactions in NVU[60]. We used human primary astrocytes throughout this study. One of

289 their roles is to sense neuronal metabolic activities and coordinate vasodilation and vasoconstriction to
290 match the blood flow accordingly[60]. Astrocytes carry out these intermediary roles through direct contact-
291 based interactions with the endothelial cells[60]. In our chip, oxygen and nutrients are provided only through
292 the 'blood-side' and 'CSF-side' channels so that the astrocytes in the 'brain' channel would have to
293 migrate and extend their endfoot toward the formed endothelial layer at the boundary to access the
294 nutrients, thus forming a physical contact with it. We indirectly confirmed this physical contact through
295 the immunofluorescence staining of water channel proteins encoded by Aquaporin-4 (AQP4), the most
296 abundant water channels in the brain[61]. The water channels in astrocytes are localized around astrocytic
297 endfoot in direct contact with the blood vessel under normal conditions[62] (**Fig. 4 i** & **ii**). This polarized
298 location reflects their mediating role in gaseous exchange including O_2, CO_2, and NO[63]. In inflammatory
299 conditions like ischemia, the immunoreactivity of AQP4 in astrocytes bleeds away from endfoot (**Fig. 4A**
300 **iii** & **iv**), implying the disruption of the mediating role of AQP4[62]. In addition, the astrocytes in the
301 ischemic samples showed the reactive astrogliosis[64] , characterized by abnormal hypertrophy (**Fig. 4A v**
302 **- vii**), massive proliferation, and upregulated Glial Fibrillary Acidic Protein (GFAP) expression levels
303 (**Fig. 4A viii**). Astrocytes failed to show these behaviors in the traditional 2D culture conditions (**Fig. S7**
304 in S.I.). The gene expression pattern (**Fig. 4A ix**) reveals a heterogeneous population of astrocytes mixed
305 with both A1 (inflammation-induced) and A2 (ischemia-induced) phenotypes (***Astrocyte reactive markers***
306 groups), as reported in *in vivo* stroke models[65]. The activated astrocytes in turn decreased their trophic
307 support for the neurons in our ischemic stroke model (***AC-neuron interaction*** group), consistent with the
308 reports from other stroke models[64].

309 ***Microglia*** are the resident macrophages and the only immune cell type in the brain[66]. Due to the
310 issues of reliable batch-to-batch reproducibility with human primary microglia, we used a transformed
311 human microglial cell line (HMC3, ATCC). Microglia in the brain show immediate pro-inflammatory
312 responses to any injury or infection[66]. Once activated, their pro-inflammatory morphology changes are
313 signified by the retraction and thickening of the processes, and the hypertrophy of the cell body[66], which
314 was successfully reproduced in our ischemic samples (**Fig. 4B i-iii**). They also promptly secrete
315 interleukin-1β (IL-1β), one of the pro-inflammatory (M1) phenotype markers, within a few hours of the
316 inflammation onset[67-69]. This upregulation of IL-1β, though, is only temporary and not sustained[67-69]. On
317 the other hand, the expression of the cluster of differentiation 68 (CD68) and ionized calcium-binding
318 adapter molecule 1 (IBA-1) is upregulated during M1 phase and persists throughout the anti-inflammatory
319 (M2) phase thereafter[67-69]. We observed these *in vivo*-like temporal patterns of the IL-1β and CD68
320 immunoreactivity in our stroke model (**Fig. 4B iv-xi**). In contrast, the traditional 2D culture conditions
321 failed to induce these behavior changes in microglia (**Fig. S8** in S.I.). The gene expression pattern of the
322 ***microglia reactive markers*** group in **Figure 4B xii** indicate that the ischemic onset led to the upregulation
323 of both pro- (M1 phenotype) and anti-inflammatory (M2a and M2b phenotypes) microglial markers, as
324 observed in *in vivo* studies[70]. Both M2a and M2b are involved in phagocytosis and produce anti-
325 inflammatory cytokines, although their activation signal pathways are distinct from each other[71]. In
326 contrast, M2c phenotype, usually regarded as a marker for the deactivating stage[71], barely appeared in the
327 24-hour time frame after the ischemic onset in our stroke model, consistent with the report [72] that M2c
328 macrophages appeared only after the downregulation of the inflammation. Many other ***Immune receptors***
329 *and* ***Chemoattractants*** also showed upregulated expression level. The genes engaging both the innate and
330 the adaptive immune responses were generally upregulated in our ischemic condition (groups from ***TLR***
331 ***signal*** to ***MHC class II mol.***), as previously reported[73]. The gene expression of the purinergic receptors,

involved in both immune cell regulation[74] and neurogenesis[75], appeared rather inconsistent (***Purinergic receptors*** group), although it was also clear that the overall immune responses were not well-regulated right after ischemia (***Immune regulation***). These gene expression alterations indicate that the ischemic insult triggered a broad spectrum of immune responses, from exacerbating the ischemic injury to helping repair, as observed in other ischemic stroke models[70].

Characterizing the neurorestorative potential of stem cells

Substantial amount of studies has supported the neurorestorative potential of stem cells for stroke treatment, but there have also been a few reports contradicting some of these observations[2,76]. This could be partially because the experiments were all conducted under different conditions and/or focusing on different aspects of the complicated recovery processes. Being an *in vitro* system, our stroke model allows for the identical experimental conditions across large number of samples and over repetitions. It thus serves as an effective platform to systematically examine the neurorestorative capacity of clinically relevant stem cells. The stem cells examined in our stroke model include human induced pluripotent stem cell derived neural progenitor cells (hNPC), human embryonic stem cell derived neural stem cells (hNSC), human hematopoietic stem cells (hHSC), bone marrow derived mesenchymal stromal/stem cells (hBMSC), adipose derived mesenchymal stromal/stem cells (hAMSC), and endothelial cell progenitor cells (hEPC). We also examined the effect of reperfusion treatment only, without stem cells, by re-introducing oxygen and glucose after ischemic insult.

The neuro-restoration after ischemic stroke entails an expansive series of processes from neural cell regeneration and immune suppression, to restoration of vascular structures, and to recovery of heterocellular interactions in NVU[38]. We selected 123 relevant genes involved in each of these aspects based on the Human Neurogenesis PCR array (Qiagen) as well as our own experimental data on the ischemic responses in our chip (**Fig. 5A i**). The details on the relevant functions of the selected genes and the corresponding references are presented in **Table S2** & **S3** in S.I. **Figure 5A i** & **ii** show the gene expression alteration by stem cells and the related Gene Ontology (GO) terms based on the STRING database of protein-protein association networks[77] (available at https://string-db.org/). The first three GO terms in **Figure 5A ii** represent more general function (*System development* (GO:0048731)*, Biological regulation* (GO:0065007) and *Response to stimulus* (GO:0050896)) and are common to all the genes chosen for our study. The overall gene expression of the chosen set was generally upregulated by the incorporation of all types of stem cells as well as the reperfusion only (**Fig. 5A iii** & **iv**). When we considered the genes with over 4-fold changes in expression, hNPC and hNSC were mostly associated with strongly upregulated genes, while the opposite was true for hBMSC (**Fig. 5A iv**). hEPC turned up almost equal numbers of strongly up- and down-regulated genes (**Fig. 5A iv**).

The stem cell incorporation as well as reperfusion generally invoked positive influence on the generation of the cells in the nervous system (*Neurogenesis*; GO term ID #: 002208), although the extent of this influence varied across stem cell types (**Fig. 5A iii**). In addition, all groups enhanced the expression of genes involved in *Neuron migration* (GO:0001764), *Neuron differentiation* (GO:0030182), *Neuron fate commitment* (GO: 0042055), *Axonogenesis* (GO:0007409), and *Gliogenesis* (GO:0042063), although hBMSC also showed inhibiting influence on *Neuron differentiation* and *Neuron fate commitment*. Notably, the reperfusion upregulated the expression of all the genes involved in neuronal migration, even though the extent was weak (**Fig. 5A iii**). As for the synapse responses, similar pattern is revealed in *Synapse organization* (GO:0007410) and *Regulation of synapse plasticity* (GO:00450808), with

374 dominantly positive influence from all experimental group, except for the fact that hEPC and reperfusion
375 exhibited equally strong enhancing and inhibiting effects.
376 In the post-stroke recovery process, it is also important to suppress the inflammation initiated by
377 the ischemia[38]. The hNPC and hNSC most strongly upregulated inflammation-related genes
378 (*Inflammation response*, GO: 0006954). While hAMSC also slightly upregulated, hAMSC, hBMSC,
379 hHSC and perfusion slightly suppressed the genes in *Inflammation response* group. To examine more
380 specific inflammatory responses, we measured the expression of glial phenotype markers (colored letters
381 in **Fig. 5A i**; a magnified heatmap is presented in **Fig. S9** in S.I.) and examined the influence of the
382 translated stem cells on their inflammatory behaviors. As for the effects on BMEC (red letters in **Fig. 5A**
383 **i** and **Fig. S9** in S.I.), hNPC, hNSC and hEPC upregulated the expression of the tight junction protein 1
384 (TJP1), but the expression of the Claudin 5 (CLDN5) was downregulated in all groups, despite the fact
385 that TJP1 and CLDN5 interact closely to form BBB[50]. The expression of PECAM1, one of the endothelial
386 adhesion molecules responsible for immune cell recruiting after brain injury[54], was all effectively
387 downregulated. As for the effects on pericytes (yellow letters in **Fig. 5A i** and **Fig. S9** in S.I.), only hAMSC
388 suppressed the expression of a reactive pericyte marker, CSPG4. The expression of CD248, involved in
389 the role of pericytes in mediating angiogenesis[78], was upregulated by hNSC and hAMSC only, and
390 generally suppressed by the rest. Regarding the influence on the microglial activities (green letters in **Fig.**
391 **5A i** and **Fig. S9** in S.I.), all groups failed to suppress the expression of a microglial reactive marker,
392 CD68, usually upregulated throughout the whole inflammatory phase[67-69]. In contrast, CD 86, a
393 proinflammatory M1 phenotype marker was successfully suppressed by all groups, except for hAMSC
394 and hHSC. hHSC enhanced the expression of CD206, an anti-inflammatory M2a phenotype marker, while
395 hEPC and hBMSC promoted the expression of CD32a, an anti-inflammatory M2b phenotype marker.
396 hBMSC, hAMSC and reperfusion upregulated the expression of CD163, a microglia-deactivating
397 phenotype marker. As for the effects on astrocytes (purple letters in **Fig. 5A i** and **Fig. S9** in S.I.), there
398 was no group suppressing the expression of VIM, a pan reactive astrocyte marker. hNPC was the only one
399 that successfully suppressed the expression of C3, an A1(inflammation) reactive astrocyte marker. In all
400 groups, the expression of CD109, a A2 (ischemia) reactive astrocyte marker, was downregulated. Taken
401 together, the expression pattern of these astrocyte reactive markers suggests that 7 days after the ischemic
402 insult there was little influence from the ischemia itself, and yet the astrocytes still retained their
403 inflammatory behaviors. The expression of IFITM3, involved in a neurotrophic support of astrocytes, was
404 upregulated in all groups, while the expression of FABP7, another gene with similar function, was
405 upregulated only by hNPC, hEPC, and hBMSC. The complexity in the overall gene expression pattern
406 suggests that all six types of stem cells as well as reperfusion have their own pathways to suppress the
407 neuroinflammation induced by the ischemia.
408 When the gene expression pattern was hierarchically clustered (Agglomerative hierarchical
409 clustering based on Euclidian distances, XLSTAT program, Addinsoft), hNPC and hNSC, with more
410 restricted fate commitment to neural cells, stood out as a group separate from the rest (the dendrogram in
411 **Fig. 5A i**). The differential expression analysis between the two groups (**Fig. 5B i,** group with neural
412 differential capacity (NDC) vs. group without NDC) identified 27 genes. We performed the GO
413 enrichment analysis on the identified genes based on the STRING database[77] and found that the stem cells
414 with NDC were beneficial in *Neurogenesis* (GO:0022008) and other closely related GO terms (**Fig. 5B**
415 **ii**). The stem cells with NDC also had positive effects on regulating the signal cascade of Mitogen-

416 Activated Protein Kinase (MAPK) (GO:0043408), an important regulator of ischemic and hemorrhagic
417 cerebral vascular disease[79].
418 To better distinguish the neurorestorative characteristics of each type of the stem cells, we
419 performed the GO enrichment analysis focusing on the genes with over four-fold expression changes after
420 stem cell incorporation to identify the dominant therapeutic pathways for each stem cell type (**Fig. 5C**).
421 The detailed GO terms are shown in **Figure S10** in S.I. Each GO term, represented by a circle, is placed
422 according to the functional hierarchy, with sub-trees grouped together under the parent GO term circle.
423 The size of a circle indicates the significance of the stem cell influence on the given GO term. Positive
424 influence/upregulation is denoted in color red while the negative influence/downregulation is denoted in
425 blue. hNPC showed the greatest potential for *Neurogenesis* (GO:0022008), especially regarding the
426 *Generation of neurons* (GO:0048699) (**Fig. 5C i**), though it had stimulating effects on other restorative
427 functions as well. The influence hNSC is more evenly spread out across diverse aspects, such as forming
428 and maturing tissue structures (*Anatomical structure development*, GO:0048856) and developing
429 multicellular organism (*Multicellular organism development*, GO:0007275) (**Fig. 5C ii**). hNSC also
430 showed strong capacity in developing blood vessel (GO:0001568), a fundamental environment for
431 restoring NVU function, as well as promoting the movement of cells (*Locomotion*, GO:0040011), an
432 important feature for reorganizing the ischemically damaged structure (**Fig. 5C ii**). Other relative
433 advantages of hNSC included enhanced adaptation to environmental changes (*Response to stimulus*,
434 GO:0050896), and better regulation of immune responses (*Regulation of immune system process* and
435 *immune response*, GO:0002682 and GO:0050776, respectively) (**Fig. 5C ii**). Notably, hNSC strongly
436 suppressed the acute inflammatory responses (*Acute-phase response,* GO:0006953) (**Fig. 5C ii**). hNSC
437 was also least associated with the *Pathways in cancer* (hsa05200 in **Fig. S10**) based on the Kyoto
438 Encyclopedia of Genes and Genomes (KEGG) database[80]. Across the whole range of the GO terms, hEPC
439 exhibited the tendency of simultaneous promotion and inhibition (**Fig. 5C iii**), while hBMSC consistently
440 inhibited most of them (**Fig. 5C iv**).
441 Compared to the top three influential stem cell types (hNPC, hNSC, and hEPC), the rest of the
442 experimental groups (hBMSC, hAMSC, hHSC, and reperfusion therapy) induced relatively smaller
443 changes in gene expression. Thus we also performed the GO enrichment analysis on the genes with over
444 two-fold expression changes for these groups (**Fig. S11** in S.I.). Unlike the distinct characteristics emerged
445 from the previous analysis for the three most influential stem cell types (**Fig. 5C** and **Fig. S10** in S.I.),
446 these groups exhibited relatively inconsistent influences over the GO terms grouped together for related
447 functions (**Fig. S11** in S.I.). A few consistent trends spotted were *Neurogenesis* promotion by hHSC and
448 *Vasculature development* (GO:0001944) inhibition by hAMSC and reperfusion.
449 We further examined the synaptic activities as an important and reliable parameter to estimate the
450 extent of the post-stroke recovery[81] (**Fig. S12**). Based on the GO enrichment analysis on the genes with at
451 least 4-fold or 2-fold expression changes, we compared the significance of the GO terms related with the
452 synapse and neurotransmitter, and examined how much each stem cell type promoted the synaptic
453 activities. This analysis also revealed a streak of strong positive effects of hNSC on many aspects of the
454 neurorestoration at synapse level: *Synapse Organization* (GO:0050808) and *Synaptic Transmission*
455 (GO:0007268), as well as the regulation of the transmission pathways of the relevant neurotransmitters
456 such as *Glutamate* (GO:0035249), *Acetylcholine* (GO:0007271), and *GABA* (GO:003228). Given the
457 molecular and functional complexity of the synapses and the importance of their coordination in

458 neurological functions[82], hNSC stand out as the highly promising therapeutic agent among all stem cells
459 evaluated in our system.

460 ***Tracking the transplanted stem cells***

461 Although the exact mechanism underlying the neurorestorative effects of the transplanted stem
462 cells for stroke is still unknown[38], there are accumulating evidences that the therapeutic effects of stem
463 cell therapies are mediated by indirect mechanisms, such as releasing trophic factors and immune
464 regulatory cytokines, promoting endogenous stem cell migration, and enhancing endogenous neural
465 plasticity and function recovery[3]. However, albeit rarely, there also have been reports that the transplanted
466 stem cells directly replace the host cells, reconstituting the damaged neural circuitry[38,83]. The primary
467 factor attracting the stem cells toward the infarcted brain parenchyma seems to be the inflammatory
468 responses of NVU[84], such as the upregulation of cytokines, CAM, and MMP, which is observed in our
469 NVU model as well.

470 With our stroke model, we were able to track the transplanted stem cells and assess the extent of
471 the direct cell replacement. We examined each of the major indicators of the cell replacement: the extent
472 of adhesion to the BBB, the number of surviving cells, the extent of infiltration into the 'brain' channel
473 and differentiation into various neural cell types in NVU. We first prepared GFP-expressing stem cells
474 using lentiviral factors. The transfection efficiency for this process is presented in **Figure S13** in S.I. The
475 number of stem cells initially adhering on the BBB was less than 5 % of the total cell number in the chip
476 in most cases (**Fig. 6A i** & **6B i** and **Fig. S14** in S.I.). After seven days of stem cell injection, the cell
477 viability counts for those attached to the BBB were in general either decreased (hNPC, hNSC, and hHSC)
478 or only slightly increased (hBMSC and hAMSC) (**Fig. 6A i** & **6B ii** and **Fig. S14** in S.I.). hEPC, in contrast,
479 vigorously proliferated and infiltrated into the 'brain' channel (**Fig. 6A i** and **6B ii** & **iii**). At the same time
480 point, seven days after transplantation, all of these transplanted stem cells barely expressed their stem cell
481 markers (**Fig. 6A ii**) that they originally expressed in 2D cultures (**Fig. S15** in S.I.). This does not mean
482 they successfully completed differentiation by that time because only very limited number of the cells
483 were mature enough to express the markers of their predicted lineages (**Fig. 6A iii** & **6B iv**). Only hNPC
484 and hNSC showed detectable neural differentiation and even those were less than 0.01% of the total cell
485 number in the chip. The extremely limited stem cell differentiation suggests that the direct cell replacement
486 is not a major mechanism underlying the neurorestorative effects of stem cell therapy, adding to the recent
487 growing evidences against it[3].

488

489 **DISCUSSION**

490 In this work, we presented a novel microphysiological stroke model to systematically evaluate the
491 efficacy of stem cell therapy. Our data revealed three key aspects of NVU microenvironments required
492 for *in vivo*-like behaviors of the constituent cells: the formation of intact BBB, the heterocellular network,
493 and the proper mechanical stimuli by blood flow (**Fig. 1**). The brain-like microenvironment ensures the
494 cells in our model to retain their native behaviors and to show clinically relevant responses to an ischemic
495 insult (**Fig. 2**, **3** & **4**). Our model served as an efficient screening platform to examine the neurorestorative
496 potential of the stem cells used in pre-clinical trials. We systematically analyzed how each type of stem
497 cells influenced the gene activities during the complicated disease progression and recovery processes
498 (**Fig. 5**). We also utilized our stroke model to track the stem cell behaviors transplanted in the ischemically
499 damaged NVU (**Fig. 6**).

Our microfluidic chip design well suited the need of establishing a functional BBB and at the same time enabled the real-time monitoring of the transplanted stem cells moving across the BBB. Similar chip designs have been proposed to build a functional BBB: positioning cells side-by-side by using micro-poles (AIM Biotech)[85] or a flow-guiding structure (PhaseGuide ™ technology, Mimetas)[10]. The design of such a chip is useful for observing the behavior of drugs or cells passing through the BBB in a 3D environment. Another mainstream in BBB chip design is to vertically stack hierarchical tissue structures between porous membranes[12,23]. The chips with this design are also commercially available (Emulate, Inc.), and have been successfully utilized to reconstruct functional BBB[84,85]. This design poses challenges to visualize the heterocellular interactions across vertical layers, necessitating confocal imaging. Moreover, the cellular interactions are inevitably interfered by the porous membranes. The advantage of this chip design is that the BBB is formed on a 2D membrane so that the dynamics of the endothelium can be monitored in the same focal plane of optical microscopes. What differentiates our design is the absence of physical structures between two neighboring channels, which allows for the cellular interactions free from any potential interference due to physical structures. We acknowledge, however, a couple of limitations of our chip design. First, the new design involves different heights and thus reduces the possible contact surface for the cells in the neighboring channels to interact with. Second, the use of a generic hydrogel whose components are not fully defined made it difficult to characterize the dynamics in the extra cellular matrix, especially the basement membrane in BBB that actively participates in BBB regulation[88]. Third, our current model uses PDMS (poly-dimethyl siloxane) and thus retains the PDMS-inherent pitfalls, such as cytotoxicity, protein uptake and gas passage[89,90]. As an alternative, microfluidic chips prepared with plastic injection molding has been proposed to overcome these limitations of PDMS, as well as for large-scale production purposes[91]. Our chip design without microstructures should be compatible with the injection molding and the combined methodology would be ideal for industrial-scale mass production.

Our stroke model successfully delineated the neurorestorative behaviors of each candidate stem cell type for stroke treatment (**Fig. 5**). The benefits of hNPC and hNSC, the stem cells with the capacity to differentiate into neural cells, consistently stood out in many aspects related with the post-stroke recovery processes. Our iPSC-derived hNPC (Millipore, Cat. No.: SCC035) were tested by the manufacturer to ensure more than 80% of their progeny to differentiate into neuronal cells. The hNSC used in this work were initially isolated from fetal cortical brain tissue at 13.5 weeks gestation (M031 clone) and classified as neural stem cells due to their ability to self-renew and produce progeny cells differentiating into neural cells[92]. Based on our GO analysis, hNPC showed the strongest capacity in generating neurons (GO:0048699) and hNSC exhibited compelling positive effects on the overall structural and functional integrity in NVU. Notably, the recovery of NVU functionality, such as gliogenesis (GO:0050767), blood vessel development (GO:001944) and immune system process (GO:0002376), was also linked with the enhanced synaptic activities, both mediated by hNSC. Given the importance of the synaptic activities in rewiring neuronal network and neurological functions, this result suggests that restoring the overall NVU functionality may be more critical for stroke treatment than replenishing neurons themselves. It is important to take into account the limitations of our approach as well when interpreting these results. First, our efficacy evaluation focused only on the gene level, as represented by GO functional analysis, and did not cover the entire range of interactions across different levels associated with post-stroke recovery. Second, the contribution from the peripheral immune cells crossing BBB was not addressed in our model and they could also play important roles in the post-

ischemic inflammation[93]. Third, since the flow in our chip was bidirectional, generated by a rocking shaker, the endothelial cells would activate different signal pathways of mechanotransduction compared to the unidirectional blood flow *in vivo*[94,95].

The results from tracking the transplanted stem cells (**Fig. 6**) suggest that the therapeutic effects of the stem cells arise mainly through the indirect mechanism of supporting the endogenous recovery, rather than direct cell replacement. At the time of gene expression alteration analysis, the number of stem cells left in our samples was mostly less than 1% of the whole cell population. The presence of such a small population itself could not possibly be the major driving force to induce the observed magnitude-fold changes in the gene expression for the whole cell population. This implies that the presence of the remaining stem cells themselves have had a minor influence on efficacy evaluation. Similar observations were reported in both animal models and clinics that the transplanted stem cells barely reached the ischemic region, but still induced significant therapeutic effects[96]. Based on these observations and implications, the pre-clinical evaluation of the candidate stem cells for cell therapy would be more effective and relevant if focusing on their capacity of restoring the damaged NVU both structurally and functionally, rather than tracing the fate of the transplanted stem cells themselves *in vivo*.

Many of the previous studies have presented conflicting results, not only on the neurorestorative potential of each stem cell type in varying conditions, but also on the mechanism by which stem cells exert their therapeutic effects[76]. The possible reason for these controversies could be the fact that the efficacy evaluation was focused only on a few aspects, lacking comprehensive analysis on the overall recovery process. Another reason could be the comorbidities often accompanying stroke, such as hypertension, high cholesterol, and diabetes, that complicate the disease progression and treatment. As such, stem cell therapy would be most effective with personalized approach based on the comprehensive health condition of individual patients. We expect that *in vitro* stroke models, like the one presented in this study, would serve as an ideal platform to develop personalized stem cell therapies, by utilizing patient-derived cells and simulating the unique pathophysiological condition of individual patients. The personalized stroke model could in turn serve as an efficient test-bed to screen many different candidate stem cells and identify the optimal stem cell regimen for the given patient. Multiomics approach, presented in some of the recent studies[97], could further expand our understanding of the post-stroke neurorestoration process and our *in vitro* stroke model is readily applicable for that purpose as well.

Taken together, our approach successfully recapitulated the NVU behaviors in the normal and ischemic conditions *in vitro* and enabled efficient and systematic evaluation of the stem cell therapy, overcoming the limitations of both the animal models and the currently available *in vitro* models. The findings from this study, especially the characterization of the neurorestorative potential of various stem cells, can steer the direction of the advanced stem cell therapeutics in research as well as in clinics. The experimental platform presented in this work is also immediately applicable to a wide range of other diseases associated with the vasculature, opening up new possibilities in the field of precision medicine.

METHODS

Cell culture

NVU constituent cells

Human primary astrocytes (ScienCell, Cat. No.: 1800) were cultured on T75 pre-coated flask with 2% poly-L-lysine solution (Sigma) in an astrocyte medium (AM) (ScienCell, Cat. No.: 1801).

585 Transformed human microglial cell line (HMC3, ATCC, Cat. No.: CRL-3304) was maintained in Eagle's
586 Minimum Essential Medium (EMEM, ATCC) containing 10% fetal bovine serum (FBS) and 1%
587 penicillin/streptomycin. Human induced pluripotent stem cell (hiPSC)-derived neural progenitor cells
588 (hNPCs) (Millipore, Cat. No.: SCC035) were maintained on T75 pre-coated flask with 1% Matrigel (BD
589 Matrigel Matrix High Concentration) in NEM. Human primary brain microvascular endothelial cells
590 (BMEC) (ScienCell, Cat. No.: 1000) were cultured on T75 pre-coated flask with 2% collagen solution
591 (Sigma) in an endothelial cell medium (ECM) (ScienCell, Cat. No.: 1001). Human brain vascular pericytes
592 (ScienCell, Cat. No.: 1200) were grown on T75 pre-coated flask with 2% poly-L-lysine solution (Sigma)
593 in a pericyte medium (PM) (ScienCell, Cat. No.: 1201). T75 Flasks coated with Matrigel and poly-L-
594 lysine solution were prepared through incubation at 37 ºC for 1 h and overnight respectively. T75 flasks
595 coated with collagen were prepared through incubation at 4 ºC overnight.

596 ***Stem cells***

597 Human endothelial progenitor cells (hEPC) were purchased from Celprogen (San Pedro, Cat. No.:
598 37089-01) and were expanded on T75 flasks pre-coated with ECM (Celprogen, Cat. No.: E36053-05-T75)
599 in complete hEPC growth medium (Celprogen, Cat. No.: M36053-05ES). Human bone marrow-derived
600 mesenchymal stem cells (hBMSC, Gibco, Cat. No.: A15652) and human adipose-derived mesenchymal
601 stem cells (hAMSC, Gibco, Cat. No.: PCS-500-011) were maintained in a mesenchymal stem cell medium
602 (MSCM) (ScienCell, Cat. No.: 7501). Human neural stem cells (hNSC, NR1), initially isolated from fetal
603 cortical brain tissue at 13.5 weeks gestation (M031 clone) and derived from the embryonic stem cell line
604 H9, were cultured in the same condition as the hiPSC-derived NSC. Human hematopoietic stem cells
605 (hHSC) were purchased from ATCC (Cat. No.: PCS-800-012) and used directly for experiments without
606 subculturing. Medium was changed every 2-3 days. Cells were passaged when the confluency reached
607 approximately 80%. 0.25% trypsin-EDTA was used to passage transformed microglia, hBMSC, and
608 hAMSC. 0.05% trypsin-EDTA was used to split astrocytes, BMEC, pericyte, hEPC, and hNSC. hNPC
609 was passaged using StemPro™ Accutase™ Cell Dissociation Reagent (Gibco, Cat. No.: A1110501).

610 **Microfluidic chip design and fabrication**

611 The master mold of microfluidic chips was fabricated using a stereolithography (UV- curing) 3D
612 printer (**Fig. S2**, Titan HD, Kudo3D Inc.). Our master mold could be prepared by most 3D printers
613 commercially available, just as many other types of microfluidic chips were successfully constructed using
614 3D printers[98]. The printed molds were extensively washed with 99% isopropyl alcohol to remove
615 unreacted monomers and curing agents, and incubated on a hotplate at 50ºC in a UV light chamber
616 (wavelength: 365nm and 405nm, output: 48 W) overnight. This washing process was repeated for at least
617 3 days before used for chip production. The surface of the molds then was spray-coated with silicone mold
618 release (CRC, cat. No.: 03300) and PDMS (Sylgard 182, Dow Corning) was poured on it. After heat
619 curing at 65 ºC for approximately 5 h, the solidified PDMS replica was peeled off from the mold. Holes
620 (1.5 mm in diameter) were made at both ends of each channel in the PDMS replica using a biopsy punch.
621 The PDMS replica was then bonded to precleaned microscope glass slides (Fisher Scientific) through
622 plasma treatment (Harrick Plasma, Cat. No.: PDC-32G). Microfluidic chips were UV-treated overnight
623 for sterilization before cell seeding.

624 **Reconstruction of a functional NVU chip**

625 (The simplified workflow for the sample preparation is described in **Table S1**.)

626 ***Reconstruction of brain tissue***

627 To construct functional brain tissue on our microfluidic chips, human iPSC-derived NPCs,
628 astrocytes, and microglia were embedded in a basement membrane extract (BME) hydrogel (Cultrex™
629 reduced growth factor basement membrane matrix type R1, Trevigen, Cat. No.: 3433-001-R1) and then
630 injected into the 'brain' channel of the chips. hNPCs were suspended in a neural expansion medium (NEM,
631 Millipore, Cat. No.: SCM004) supplemented with 2 mM glutamine and 0.02 μg/mL FGF-2. To obtain
632 astrocytes and microglia in their resting state, they were sustained in AM without serum and astrocyte-
633 conditioned medium (ACM, ScienCell, Cat. No.: 1811), respectively, for one day before the injection.
634 The density of the suspension for each cell type was ~ 8×10^6 cells/mL. We prepared cell mixture by
635 mixing hNPCs, astrocytes and microglia at the ratio of 8:4:1 (n/n/n) and then with BME Type R1 hydrogel
636 prepolymer (gel: cell = 4: 1 (v/v)). According to the vendor, more than 80% of the hiPSC-derived NPC
637 commit to mature neurons, making the final cell ratio for neurons, astrocytes and microglia fall in the
638 range of 5-6: 4-5: 1 (n:n:n), similar to the naïve brain [99]. The gel-cell mixture was injected into the 'brain'
639 channel of a chip placed on a cold pack. The total number of the incorporated neural cells in the 'brain'
640 channel was around 40,000. After injection, chips were transferred to rectangular 4-well cell culture plates
641 (Thermo Scientific, Cat. No.: 267061) and incubated at 37 ºC in a cell culture incubator for 30 minutes
642 for gelation. After gelation, the serum-free mixed medium of NEM, serum-free AM and ACM (8:4:1,
643 v/v/v) was injected into both the 'blood-side' and the 'CSF-side' channels and then changed every day.
644 From day 3 after the injection, NEM was replaced with a neural differentiation medium (NDM) (Millipore,
645 Cat. No.: SCM111) which generates glutamatergic neurons [100]. The culture medium was changed every
646 other day for the next 2 days until BBB reconstruction.

647 ***BBB reconstruction***

648 BMEC and human pericytes were suspended in ECM and PM respectively at the density of ~ $1 \times$
649 10^6 cells/mL. BMEC and pericytes were mixed at 9:1 (n/n) ratio based on literature [59,101] and 10 μL of the
650 cell suspension was injected into the 'blood-side' channel of a chip after the neural cells were co-cultured
651 for 4 days in the 'brain' channel. The total cell number in the 'blood-side' channel was around 10,000.
652 We tilted the chip a little bit for BMEC and pericytes to adhere to the side wall of the hydrogel in the 'brain'
653 channel and incubated it for 3 hours. Then we removed old medium and injected fresh mixed medium
654 (ECM: PM = 9:1 (v/v), final serum content of 4.7% (v/v)) into the 'blood-side' channel to remove any
655 unattached cells and debris. We changed the mixed medium of ECM and PM in the 'blood-side' channel
656 and the mixed medium of NDM, AM and ACM in the 'CSF-side' channel every other day. Chips were
657 cultured for 3 more days for BBB formation. In the experiments to track pericytes, BMECs and pericytes
658 were pre-stained with DiD and DiO cell-labelling solution (Vybrant ™, Invitrogen), respectively, whole
659 their nuclei were counterstained with NucBlue™ Live ReadyProbes™ Reagent (Thermo Fisher
660 Scientific).

661 ***Shear stress on the BBB***

662 To apply the shear stress of flow in the physiological range as in the brain microvasculature (0.01 –
663 10 dyne/cm^2) [102], we generated a pulsatile bidirectional flow by placing the samples on a rocking see-saw
664 shaker (Mimetas, OrganoFlow® L,). We adopted the flow condition of a previous work [10] in which a
665 functional BBB was successfully established. We modulated the design parameters of our model based
666 on the equation below:

667 $$\tau = \frac{6 \cdot Q \cdot \mu}{b \cdot h^2}$$

, where τ = shear stress (dyne/cm^2), Q = flow rate (cc/s), μ = viscosity of culture medium, b = channel width, and h = channel height. Based on the Poiseuille's law,

$$Q = \frac{\Delta P \cdot \pi \cdot D^4}{128 \cdot \mu \cdot L}$$

$$D = \frac{2 \cdot h \cdot b}{h + b} \quad \text{(hydraulic diameter of a rectangular channel)}$$

, where $\Delta P = \rho \cdot L \cdot \sin\theta$ (pressure difference between the inlet and outlet), θ = tilt angle of a shaker, L = channel length, ρ = liquid density. The mean shear stress during a given time period is proportional to the following parameters:

$$\tau \propto \frac{h^2 \cdot b^3}{(h+b)^4} \cdot \sin\theta$$

In the previous works [10,103] with the experimental setup with h = 220 μm, b = 400 μm, θ = 7°, and the tilting frequency of 16 minutes, an oscillating and non-uniform flow generated 1.7 dyne/cm^2 of the maximum shear stress. Our setup with h = 400 μm, b = 1 mm, θ = 4°, and the tilting frequency of 1 minute was expected to generate 3.4 dyne/cm^2 of the maximum shear stress at a higher frequency.

Induction of *in vitro* ischemic condition

To induce ischemia, the chips were placed in the incubation chamber of an EVOS fl auto imaging system with 2% O_2 and 5% CO_2 for 24 hours [34]. Before the chips were incubated in the hypoxic chamber, the media was replaced to serum- and glucose-free DMEM (Gibco, Cat. No.: 11966025) stored at the same hypoxic condition (2% O_2 and 5% CO_2) for 24 hours before use. There was no flow during the ischemic period.

Measurement of cell viability and cytotoxicity

Cell viabilities and cytotoxicity were measured using Live/Dead™ Viability kit (ThermoFisher Scientific, Cat. No.: L3224) and LDH-Cytox Assay™ kit (BioLegend, Cat. No.: 426401), respectively. Cell viability was calculated as the number of viable cells divided by the total number of cells. The relative cytotoxicity of the ischemia was calculated based on the optical densities (OD) read at a wavelength of 490 nm as follows: $Cytotoxicity = \frac{OD_{ischemic\ sample} - OD_{normoxic\ sample}}{OD_{whole\ cell\ lysate} - OD_{normoxic\ sample}}$.

Functional characterization of the reconstructed BBB

Evaluation of BBB as a physically intact barrier

To evaluate the physical intactness of the formed BBB in a microfluidic chip, we injected a FITC-conjugated dextran (70 kDa and 4 kDa) to the 'blood-side' channel and monitored their diffusion across it. We took fluorescence images (at 488 nm) at different time points in one hour after the probe injection and the fluorescence intensities were measured with ImageJ (NIH). The permeability coefficients were calculated by the equation[104-108] below.

$$P_{app} = \frac{1}{A \cdot C_0} \cdot \frac{dQ}{dt} \cong \frac{1}{A \cdot (\bar{I}_o^{blood} - \bar{I}_o^{brain})} \cdot \frac{V^{brain} \cdot \Delta\bar{I}^{brain}}{\Delta t}$$

A = the surface area of the membrane, C_0 = initial concentration on the donor side, $\frac{dQ}{dt}$ = the transport rate.
V^{brain}= hydrogel volume in the 'brain' channel, $\bar{I}^{brain}$= mean fluorescence intensity in the 'brain' channel,
$\bar{I}^{blood}$= mean fluorescence intensity in the 'blood-side' channel, I_o= initial fluorescence intensity

706
707 This equation assumes that flux across the imaging boundary is negligible, and transendothelial flux is
708 constant[105]. In our chip these assumptions were safely met for the time intervals (Δt) shorter than 15
709 minutes; i.e. there were no significant difference between P_{app} calculated with 5, 10 and 15 minutes of Δt
710 (n = 5, p-value > 0.05). Δt was set to 10 minutes. We calculated the P_{app} of the BBB (P_{app}^{endo}) based on the
711 P_{app} of the whole barrier ($P_{app}^{whole\ barrier}$)and the endothelium itself ($P_{app}^{hydrogel}$) using the following
712 equation.

713 $$\frac{1}{P_{app}^{whole\ barrier}} = \frac{1}{P_{app}^{hydrogel}} + \frac{1}{P_{app}^{endo}}$$

714 ***Evaluation of BBB as a bio-chemically intact barrier***

715 We examined whether the formed endothelium could isolate the neural cells in the 'brain' channel
716 from the serum in the 'blood-side' channel. First, we added the serum-containing medium of ECM and
717 PM (9:1, v/v) containing 10% FBS into the 'blood-side' channel. After incubation for 24 h, we studied
718 microglia behavior by immunostaining them with its reactive marker, ionized calcium-binding adapter
719 molecule 1 (IBA-1), and its activation marker, differentiation 68 (CD68).

720 ***Evaluation of BBB as a cell-selective barrier to invading cells***

721 We examined whether the reconstructed BBB could show distinct responses to different types of
722 invading cells; two types of human breast cancer cell lines were tested for this purpose: MB-231 and its
723 brain metastatic derivative population, MB-231Br. The MB-231Br was provided by Dr. Joan Massagué
724 at Memorial Sloan Kettering Cancer Center. The cells were prestained with Vybrant™ DiO cell-labeling
725 solution (Invitrogen, Cat. No.: V22886). For prestaining, cells were incubated with staining medium (5
726 μL labelling solution per 1 mL culture medium) for 20 min in a cell culture incubator and washed with
727 sterile PBS (Phosphate-buffered saline, pH = 7.4) for 3 times. And 10 μL of the cells were injected into
728 the 'blood-side' channel at 1×10^6 cells/mL density. We tilted the chip a little bit so that the cells could
729 pile up on the hydrogel border. Images were taken 1 day or 10 days after the cancer cell injection using
730 an EVOS fl auto imaging system (Life Technologies).

731 **Neuronal degeneration staining**

732 Neuronal degeneration induced by ischemia was studied using Fluoro-Jade C (FJC) Staining Kit
733 according to the manufacture's protocol (Biosensis, biosensis® Ready-to-Dilute (RTD) TM Fluoro-Jade®
734 C Staining Kit, Cat. No.: TR-100-FJ) with some modifications. To make sure staining solutions diffuse
735 well into the hydrogel in the middle channel of the chips where neurons were growing, incubation time of
736 staining solutions on the protocol were tripled in our experiments. After staining, samples were washed at
737 least three times with PBS. For each wash, the incubation time was 5 - 10 min. Images were obtained
738 with EVOS fl microscope (Life Technologies).

739 **Immunocytochemistry (ICC) of NVU chips**

740 For fixation of cells in a NVU chip, 50 - 60 μL of 4% paraformaldehyde (PFA) was added as
741 droplets onto the inlet of each channel and kept in the channels for at least 30 min. The fixed hydrogel
742 matrix was gently washed by adding 30 - 40 μL of PBS drops onto the inlet of each channel. This washing
743 was repeated at least 5 times. Then, the cells in the NVU chip were permeabilized in 0.1% Triton X-100
744 in PBS for 10 - 15 min. The permeabilized cells were washed with PBS for 5 times and then blocked with
745 5% normal donkey serum in PBST (0.05 % Tween 20 in PBS) for 40 min to 1 hr. The blocked cells were
746 incubated with primary antibodies (30 - 40 μL per channel) at least overnight at 4°C. The dilution ratio of
747 primary antibodies was as follows: sheep polyclonal anti-human CD31/PECAM-1 (R&D Systems, Cat.

748 No.: AF806, 1:20), rabbit polyclonal anti-human GFAP (Sigma, Cat. No.: G9269, 1:100), chicken
749 polyclonal anti-human GFAP (Synaptic Systems, Cat. No.: 173006, 1:500), rabbit polyclonal anti-human
750 AQP4 (Novus Biologicals, Cat. No.: NBP1-87679, 1:2000), mouse monoclonal anti-human ZO-1
751 (Invitrogen, Cat. No.: 339100, 1:100), rabbit polyclonal anti-human von Willebrand Factor (vWF, Sigma,
752 Cat. No.: F3520, 1:200), mouse monoclonal anti-human vWF (Sigma, Cat. No.: AMAB90931, 1:500),
753 mouse monoclonal anti-human podoplanin (PDPN) (E-1) (Santa Cruz Biotechnology, Cat. No.:
754 SC376695, 1:100), rabbit polyclonal anti-human Synapsin 1/2 (Synaptic System, Cat. No.: 106003,
755 1:1,000), chicken polyclonal anti-human MAP2 (Abcam, Cat. No.: ab5392, 1:10,000), goat polyclonal
756 anti-human IBA-1 (Abcam, Cat. No.: ab5076, 1:200), rabbit polyclonal anti-human IL-1β (Abcam, Cat.
757 No.: ab9722, 1:100), mouse monoclonal anti-human CD68 (Bio-Rad, Cat. No.: MAC5709, 1:100), rabbit
758 monoclonal anti-human CD44 (Invitrogen, Cat. No.: 19H8L4, 1: 500), mouse monoclonal anti-human
759 CD34 (Life technology, Cat. No.: BI-3C5, 1:250), mouse monoclonal anti-human Nestin (ThermoFisher,
760 Cat. No.: MA1-5840, 1: 250), rabbit monoclonal anti-human PDGFR β (Cell Signaling, Cat. No.: 3169,
761 1:100), and mouse monoclonal anti-human HIF-1 α (Abcam, Cat. No.: ab6066, 1:200). To prevent dryness
762 during the primary antibody incubation, the plates containing the chips were humidified with distilled
763 water. Incubated samples were washed with blocking solution for 5 times, and then various secondary
764 antibodies (Jackson ImmunoResearch Laboratories) including DyLight405 anti-rabbit, Alexa Fluor 488
765 anti-chicken, mouse, or rabbit, Alexa Fluor 594 anti-mouse, rabbit, or sheep, and Alexa Fluor 647 anti-
766 mouse, rabbit, or sheep were added to samples at a dilution of 1:500 at room temperature for at least 2 h.
767 The immunostained slides were mounted with ProLong Diamond antifade reagent (ThermoFisher) and
768 cured for 24 h. To prevent collapsing of the fixed hydrogel structure, all buffers including PFA, PBS, and
769 blocking solutions were not fully removed from the outlet reservoir throughout the whole procedure of
770 ICC.

771 **3D images of BBB**

772 Fluorescent images of immunostained-BBB structures were acquired at 10X and 20X
773 magnifications with a Zeiss LSM 880 confocal microscope. The NVU chip was scanned at different focal
774 planes ranging from Z = 0 to 100 μm with 8 - 10 μm intervals. For 3D reconstruction of images, the 3D
775 Viewer in Plugins of ImageJ was used.

776 **Calcium imaging and analysis**

777 To record the cytosolic calcium oscillation in the neurons differentiated from iPSC-derived NPC,
778 we pre-stained the iPSC-derived NPC with DiL (1,1'-Dioctadecyl-3,3,3',3'-Tetramethylindocarbocyanine
779 Perchlorate, Molecular probes, Cat. No.: D282) before incorporating with other cells in our chip, as
780 described in the process of *Reconstruction of brain tissue* and *BBB*. One hour prior to calcium imaging,
781 we added 5 μM Fluo-4 AM (Thermo Fisher Scientific, Cat. No.: F14201) to the inlets of the chips. We
782 observed spontaneous calcium oscillations in DiL labeled cells using a confocal microscope (Carl Zeiss,
783 LSM 710, Göttingen, Germany) under 37 ºC and 5 % CO_2. Calcium signaling was recorded in time-lapse
784 video recording mode at a speed of 2 sec/frame for 10 minutes. The recorded images were analyzed using
785 ImageJ software with Time Series Analyzer V3 plugin. Calcium dynamics in each DiL labeled cell was
786 traced with ROI (Region of Interest) analysis, and the parameters of calcium oscillation in each cell, such
787 as frequency and amplitude ($\Delta F/F_0$) were calculated using a custom-made script written in IDL (Interactive
788 digital language). Extracellular background signal was subtracted from the traced calcium signals, which
789 in turn were normalized to the intracellular basal line (F_0).

790 **Real-time quantitative PCR**

We evaluated the gene expression pattern of the entire cell population in our chip. More than six chips from each experimental condition were used to extract RNA for analysis. Cells from different batches were used to ensure cell numbers sufficient to prepare multiple chips simultaneously. The culture medium in both of the side channels was removed and replaced with fresh PBS. The process was repeated twice with 5 min incubation in between. After removal of PBS, 50 uL of RLT buffer plus lysis buffer (Qiagen, Cat. No.: 1053393) was injected into both of the side channels and incubated for 5 min. Thorough pipetting was needed in order to harvest all types of cells in the chip, especially those in the 'brain' channel. Total RNA was then extracted using RNeasy Mini Kit according to the manufacture's protocol (Qiagen, Cat. No.: 74104). RNA quality and concentration were determined by Agilent 210 Bioanalyzer. The RNA amount obtained from each chip was as follows for each experimental condition: a chip with 10 days under normoxia generated about 250 ng; the same condition followed by 24 hours of ischemia generated about 130 ng; a chip with 18 days under normoxia, used as the control group in neurorestorative efficacy evaluation, about 400 ng; a chip with reperfusion only, about 200 ng; a chip with transplanted stem cells, about 350 ng to 750 ng depending on the stem cell type. Total RNA was reverse transcribed to cDNA using a high-capacity cDNA reverse transcription kit (Applied Biosystems, Cat. No.: 4368814). Real-time qPCR was performed in a StepOnePlus real-time PCR system (Applied Biosystems) using SsoAdvanced Universal SYBR Green Supermix (Bio-Rad, Cat. No.: 1725272A) to quantify the expression levels of the genes of interest. qPCR amplification was achieved with 40 cycles of 30 s at 95 °C, 15 s at 95 °C, and 50 s at 65 °C. We distinguished the signal from noise using StepOnePlus real-time PCR software and further checked manually to ensure the obtained Ct values had indeed come from real signals. Customized qPCR plates were designed and fabricated by Sciencell. Neurogenesis qPCR plates were purchased from Qiagen. We first chose 12 genes with well-known ischemic behaviors and confirmed the reproducibility of their expression by triplicate. And we measured the expression of the final 123 genes with more than six independent chips for each experimental condition.

Evaluation of the neurorestorative potential of stem cells

We examined the neurorestorative potential of various types of stem cells. 24 hours after the ischemic insult, the serum- and glucose-free DMEM medium was replaced with the mixed medium of NDM, serum-free AM, and ACM (8:4:1, v/v/v) in the 'CSF-side' channel. Then the stem cells were collected at 5×10^6 cells/mL density in mixed medium of serum-containing ECM and PM (9:1, v/v) and injected into the 'blood-side' channel ($n \sim 10^4$). This setting represented the intra-vascular route for stem cell transplantation, the most widely used route for stem cell therapy [109]. The stem cells were incubated for 3 hours to allow for cell adhesion. Fresh mixed medium of ECM and PM (9:1, v/v) was then added to the 'blood-side' channel. Medium in both of the side channels was changed every day for 7 more days before further analysis.

Tracking stem cells

In order to track stem cell behaviors in the chip, we used the lentivirus vector carrying green fluorescent protein (GFP) to transfect stem cells hNPC, hNSC (NR1), hAMSC, hBMSC, and hEPC. We used pre-staining method for hHSC because the virus transfection efficiency of hHSC was not sufficient. We purchased ready-to-use GFP lentiviral particles from GenTarget Inc (San Diego, CA, USA) and used them according to the manufacture's protocol with some modification. More specifically, cells were cultured in a 48-well plate until the confluency reached 50% to 75%. Cell culture medium was removed before transduction and 0.25 mL of fresh medium and 15 μL of virus solution were added to each well. Cells were cultured in a cell culture incubator for 2 - 3 days without medium change in between to achieve

834 desirable transduction efficiency. hHSC was prestained with Vybrant™ DiO cell-labeling solution
835 (Invitrogen, Cat. No.: V22886). hHSCs at 1×10^6 cells/mL were incubated with staining medium (10 μL
836 labelling solution per 1 mL culture medium) in a 96-well plate for 20 min in a cell culture incubator and
837 washed with sterile PBS (Phosphate-buffered saline, pH = 7.4) for 3 times for use. After injecting each
838 stem cell into the 'blood-side' channel of a chip following ischemic insult, images were taken every other
839 day for up to 7 days to track stem cell infiltration. At the end of the 7 days, stem cells were immunostained
840 for stemness markers (Nestin for hNPC and hNSC, CD44 for hBMSC and hAMSC, and CD34 for hEPC
841 and hHSC) and differentiation markers (MAP2 for neurogenesis, GFAP for gliagenesis, and von
842 Willebrand Factor for vasculogenesis). The extravasation extent of both cancer and stem cells was
843 quantified by image scoring (ImageJ, NIH).

844 **Statistical Methods**

845 Every independent experiment was repeated at least three times, and the results were presented as
846 the mean ± standard deviation (SD). For the quantitative analysis of fluorescence images, we obtained at
847 least three images from different samples and used an image analysis software, ImageJ (NIH), to
848 quantitatively analyze the aspects of interest. Statistical significance was evaluated using one-sided
849 Student's t-Test for two group comparisons and one way ANOVA with Bonferroni-Holm post hoc test
850 for multiple group comparison (Daniel's XL Toolbox). P-values less than 0.05 were considered
851 significant. All data were presented as the mean ± s.d.

852 **Acknowledgement**: We are grateful to Dr. Hyejean Suh for editing the manuscript. We thank Tom Klein,
853 and Joseph and Sharon Saunders for their generous support. WL was supported by NIH National Center
854 for Advancing Translational Science Clinical and Translational Science Award at the Stanford Child
855 Health Research Institute (UL1 TR001085) and NIH/NCI career development award (K25CA201545).
856 **Author contributions**: Z.L. & K.-M.K. designed and performed the experiments, and analyzed and
857 interpreted the data; J.P. designed experiment; H.-J.J. performed the experiments; W.L. conceived and
858 supervised the project, designed and performed experiments, analyzed and interpreted the data. The
859 manuscript was mainly written by W.L. with all authors' contribution.
860 **Competing interests:** The authors declare no competing interests.
861 **Data and materials availability:** All materials and equipment are commercially available, except a breast
862 cancer cell line of MB-231Br (provided by Dr. Massagué with Materials Transfer Agreement) and a
863 hESC-derived human neural stem cell line (NR1, generated by Dr. Steinberg, one of our authors).

864

865 **References**

866 1 Wang, Y. & Cai, Y. Obtaining human ischemic stroke gene expression biomarkers from animal models: A cross-
867 species validation study. *Scientific Reports* **6**, 29693-29702 (2016).
868 2 Stonesifer, C. *et al.* Stem cell therapy for abrogating stroke-induced neuroinflammation and relevant secondary cell
869 death mechanisms. *Progress in Neurobiology* **158**, 94-131 (2017).
870 3 Wechsler, L. R., Bates, D., Stroemer, P., Andrews-Zwilling, Y. S. & Aizman, I. Cell therapy for chronic stroke. *Stroke*
871 **49**, 1066-1074 (2018).
872 4 McGonigle, P. & Ruggeri, B. Animal models of human disease: challenges in enabling translation. *Biochemical*
873 *pharmacology* **87**, 162-171 (2014).
874 5 Savitz, S. I. *et al.* Stem cells as an emerging paradigm in stroke 3: enhancing the development of clinical trials. *Stroke*
875 **45**, 634-639 (2014).
876 6 Woodruff, T. M. *et al.* Pathophysiology, treatment, and animal and cellular models of human ischemic stroke.
877 *Molecular Neurodegeneration* **6**, 11-29 (2011).
878 7 Del Zoppo, G. The neurovascular unit in the setting of stroke. *Journal of internal medicine* **267**, 156-171 (2010).
879 8 Sivandzade, F. & Cucullo, L. In-vitro blood–brain barrier modeling: a review of modern and fast-advancing
880 technologies. *Journal of Cerebral Blood Flow & Metabolism* **38**, 1667-1681 (2018).

9 Herland, A. *et al.* Distinct contributions of astrocytes and pericytes to neuroinflammation identified in a 3D human blood-brain barrier on a chip. *PLoS One* **11**, e0150360 (2016).
10 Wevers, N. R. *et al.* A perfused human blood–brain barrier on-a-chip for high-throughput assessment of barrier function and antibody transport. *Fluids and Barriers of the CNS* **15**, 23 (2018).
11 Grifno, G. N. *et al.* Tissue-engineered blood-brain barrier models via directed differentiation of human induced pluripotent stem cells. *Scientific reports* **9**, 1-13 (2019).
12 Ahn, S. I. *et al.* Microengineered human blood–brain barrier platform for understanding nanoparticle transport mechanisms. *Nature communications* **11**, 1-12 (2020).
13 Kim, S., Lee, H., Chung, M. & Jeon, N. L. Engineering of functional, perfusable 3D microvascular networks on a chip. *Lab on a Chip* **13**, 1489-1500 (2013).
14 Soofi, S. S., Last, J. A., Liliensiek, S. J., Nealey, P. F. & Murphy, C. J. The elastic modulus of Matrigel™ as determined by atomic force microscopy. *Journal of structural biology* **167**, 216-219 (2009).
15 Budday, S. *et al.* Mechanical characterization of human brain tissue. *Acta biomaterialia* **48**, 319-340 (2017).
16 Uemura, M. *et al.* Matrigel supports survival and neuronal differentiation of grafted embryonic stem cell-derived neural precursor cells. *J. Neurosci. Res.* **88**, 542-551 (2010).
17 Yu, Z. *et al.* Neuroglobin promotes neurogenesis through Wnt signaling pathway. *Cell death & disease* **9**, 945-956 (2018).
18 Nakagawa, S. *et al.* A new blood–brain barrier model using primary rat brain endothelial cells, pericytes and astrocytes. *Neurochemistry international* **54**, 253-263 (2009).
19 Dejana, E. Endothelial cell–cell junctions: happy together. *Nature reviews Molecular cell biology* **5**, 261-270 (2004).
20 Lee, C. S. & Leong, K. W. Advances in microphysiological blood-brain barrier (BBB) models towards drug delivery. *Current Opinion in Biotechnology* **66**, 78-87 (2020).
21 Mayhan, W. G. & Heistad, D. D. Permeability of blood-brain barrier to various sized molecules. *American Journal of Physiology-Heart and Circulatory Physiology* **248**, H712-H718 (1985).
22 Srinivasan, B. *et al.* TEER measurement techniques for in vitro barrier model systems. *Journal of laboratory automation* **20**, 107-126 (2015).
23 Helms, H. C. *et al.* In vitro models of the blood–brain barrier: an overview of commonly used brain endothelial cell culture models and guidelines for their use. *Journal of Cerebral Blood Flow & Metabolism* **36**, 862-890 (2016).
24 Wang, Y. I., Abaci, H. E. & Shuler, M. L. Microfluidic blood–brain barrier model provides in vivo-like barrier properties for drug permeability screening. *Biotechnology and bioengineering* **114**, 184-194 (2017).
25 Brown, J. A. *et al.* Recreating blood-brain barrier physiology and structure on chip: A novel neurovascular microfluidic bioreactor. *Biomicrofluidics* **9**, 054124 (2015).
26 Foo, L. C. *et al.* Development of a method for the purification and culture of rodent astrocytes. *Neuron* **71**, 799-811 (2011).
27 Bos, P. D. *et al.* Genes that mediate breast cancer metastasis to the brain. *Nature* **459**, 1005-1009 (2009).
28 Hakim, A. M. Ischemic penumbra: the therapeutic window. *Neurology* **51**, S44-S46 (1998).
29 Heiss, W.-D. *et al.* Progressive derangement of periinfarct viable tissue in ischemic stroke. *Journal of Cerebral Blood Flow & Metabolism* **12**, 193-203 (1992).
30 Stankowski, J. N. & Gupta, R. Therapeutic Targets for Neuroprotection in Acute Ischemic Stroke: Lost in Translation? *Antioxidants & redox signaling* **14**, 1841-1851 (2011).
31 Shi, H. Hypoxia inducible factor 1 as a therapeutic target in ischemic stroke. *Current medicinal chemistry* **16**, 4593-4600 (2009).
32 Jovanović, P. *et al.* Lactate dehydrogenase and oxidative stress activity in primary open-angle glaucoma aqueous humour. *Bosnian Journal of Basic Medical Sciences* **10**, 83 (2010).
33 Mattson, M. P., Culmsee, C. & Yu, Z. F. Apoptotic and antiapoptotic mechanisms in stroke. *Cell and tissue research* **301**, 173-187 (2000).
34 Bereczki, J., Balla, J. & Bereczki, D. Heme Oxygenase-1: Clinical Relevance in Ischemic Stroke. *Current pharmaceutical design* **24**, 2229-2235 (2018).
35 Boshuizen, M. C. & Steinberg, G. K. Stem Cell–Based Immunomodulation After Stroke: Effects on Brain Repair Processes. *Stroke* **49**, 1563-1570 (2018).
36 Jin, R., Yang, G. & Li, G. Inflammatory mechanisms in ischemic stroke: role of inflammatory cells. *Journal of leukocyte biology* **87**, 779-789 (2010).
37 Park, J. S., Bateman, M. C. & Goldberg, M. P. Rapid alterations in dendrite morphology during sublethal hypoxia or glutamate receptor activation. *Neurobiology of disease* **3**, 215-227 (1996).
38 Schmued, L. C., Albertson, C. & Slikker Jr, W. Fluoro-Jade: a novel fluorochrome for the sensitive and reliable histochemical localization of neuronal degeneration. *Brain research* **751**, 37-46 (1997).
39 Besse, A. *et al.* Personalized medicine approach confirms a milder case of ABAT deficiency. *Molecular brain* **9**, 93 (2016).
40 Okaty, B. W., Miller, M. N., Sugino, K., Hempel, C. M. & Nelson, S. B. Transcriptional and electrophysiological maturation of neocortical fast-spiking GABAergic interneurons. *Journal of Neuroscience* **29**, 7040-7052 (2009).

41 Lai, T. W., Zhang, S. & Wang, Y. T. Excitotoxicity and stroke: identifying novel targets for neuroprotection. *Progress in neurobiology* **115**, 157-188 (2014).
42 Cameron, M. *et al.* Calcium imaging of AM dyes following prolonged incubation in acute neuronal tissue. *PLoS One* **11** (2016).
43 Marambaud, P., Dreses-Werringloer, U. & Vingtdeux, V. Calcium signaling in neurodegeneration. *Molecular neurodegeneration* **4**, 20 (2009).
44 Sneyd, J. *et al.* On the dynamical structure of calcium oscillations. *Proceedings of the National Academy of Sciences* **114**, 1456-1461 (2017).
45 Arundine, M. & Tymianski, M. Molecular mechanisms of calcium-dependent neurodegeneration in excitotoxicity. *Cell calcium* **34**, 325-337 (2003).
46 Weksler, B. *et al.* Blood-brain barrier-specific properties of a human adult brain endothelial cell line. *The FASEB journal* **19**, 1872-1874 (2005).
47 Tornavaca, O. *et al.* ZO-1 controls endothelial adherens junctions, cell–cell tension, angiogenesis, and barrier formation. *Journal of Cell Biology* **208**, 821-838 (2015).
48 Mathiu, O., ávan der Meer, A. D., JungáKim, H., ávan der Helm, M. W. & den Berg, A. Measuring direct current trans-epithelial electrical resistance in organ-on-a-chip microsystems. *Lab on a Chip* **15**, 745-752 (2015).
49 Talwar, T. & Srivastava, M. V. P. Role of vascular endothelial growth factor and other growth factors in post-stroke recovery. *Annals of Indian Academy of Neurology* **17**, 1-6 (2014).
50 Sandoval, K. E. & Witt, K. A. Blood-brain barrier tight junction permeability and ischemic stroke. *Neurobiology of Disease* **32**, 200-219 (2008).
51 Carlos, T., Clark, R., Franicola-Higgins, D., Schiding, J. & Kochanek, P. Expression of endothelial adhesion molecules and recruitment of neutrophils after traumatic brain injury in rats. *Journal of leukocyte biology* **61**, 279-285 (1997).
52 DeStefano, J. G., Xu, Z. S., Williams, A. J., Yimam, N. & Searson, P. C. Effect of shear stress on iPSC-derived human brain microvascular endothelial cells (dhBMECs). *Fluids and Barriers of the CNS* **14**, 20-34 (2017).
53 Colgan, O. C. *et al.* Regulation of bovine brain microvascular endothelial tight junction assembly and barrier function by laminar shear stress. *American Journal of Physiology-Heart and Circulatory Physiology* **292**, 3190-3197 (2007).
54 Sweeney, M. D., Ayyadurai, S. & Zlokovic, B. V. Pericytes of the neurovascular unit: key functions and signaling pathways. *nature neuroscience* **19**, 771-783 (2016).
55 Winkler, E. A., Bell, R. D. & Zlokovic, B. V. Pericyte-specific expression of PDGF beta receptor in mouse models with normal and deficient PDGF beta receptor signaling. *Molecular neurodegeneration* **5**, 32 (2010).
56 Sá-Pereira, I., Brites, D. & Brito, M. A. Neurovascular unit: a focus on pericytes. *Molecular neurobiology* **45**, 327-347 (2012).
57 Abbott, N. J., Rönnbäck, L. & Hansson, E. Astrocyte–endothelial interactions at the blood–brain barrier. *Nature Reviews Neuroscience* **7**, 41-53 (2006).
58 Papadopoulos, M. C. & Verkman, A. S. Aquaporin-4 and brain edema. *Pediatric nephrology* **22**, 778-784 (2007).
59 Liddelow, S. A. *et al.* Neurotoxic reactive astrocytes are induced by activated microglia. *Nature* **541**, 481-487 (2017).
60 Kimelberg, H. K. & Nedergaard, M. Functions of astrocytes and their potential as therapeutic targets. *Neurotherapeutics* **7**, 338-353 (2010).
61 Sofroniew, M. V. & Vinters, H. V. Astrocytes: biology and pathology. *Acta neuropathologica* **119**, 7-35 (2010).
62 Liddelow, S. A. & Barres, B. A. Reactive astrocytes: production, function, and therapeutic potential. *Immunity* **46**, 957-967 (2017).
63 Guruswamy, R. & ElAli, A. Complex roles of microglial cells in ischemic stroke pathobiology: new insights and future directions. *International journal of molecular sciences* **18**, 496-511 (2017).
64 Taib, T. *et al.* Neuroinflammation, myelin and behavior: temporal patterns following mild traumatic brain injury in mice. *PloS one* **12**, e0184811 (2017).
65 Matt, S. M., Lawson, M. A. & Johnson, R. W. Aging and peripheral lipopolysaccharide can modulate epigenetic regulators and decrease IL-1β promoter DNA methylation in microglia. *Neurobiology of aging* **47**, 1-9 (2016).
66 Jalland, C. M. *et al.* Neil3 induced neurogenesis protects against prion disease during the clinical phase. *Scientific Reports* **6**, 37844-37852 (2016).
67 Patel, A. R., Ritzel, R., McCullough, L. D. & Liu, F. Microglia and ischemic stroke: a double-edged sword. *International journal of physiology, pathophysiology and pharmacology* **5**, 73-90 (2013).
68 Walker, D. G. & Lue, L.-F. Immune phenotypes of microglia in human neurodegenerative disease: challenges to detecting microglial polarization in human brains. *Alzheimer's research & therapy* **7**, 56-64 (2015).
69 Mantovani, A. *et al.* The chemokine system in diverse forms of macrophage activation and polarization. *Trends in immunology* **25**, 677-686 (2004).
70 Picascia, A., Grimaldi, V., Iannone, C., Soricelli, A. & Napoli, C. Innate and adaptive immune response in stroke: focus on epigenetic regulation. *Journal of neuroimmunology* **289**, 111-120 (2015).
71 Junger, W. G. Immune cell regulation by autocrine purinergic signalling. *Nature Reviews Immunology* **11**, 201-212 (2011).

72 Oliveira, A., Illes, P. & Ulrich, H. Purinergic receptors in embryonic and adult neurogenesis. *Neuropharmacology* **104**, 272-281 (2016).
73 Marei, H. E. M. Potential of stem cell-based therapy for ischemic stroke. *Frontiers in Neurology* **9**, 34-40 (2018).
74 Szklarczyk, D. *et al.* Protein-protein association networks with increased coverage, supporting functional discovery in genome-wide experimental datasets. *Nucleic acids research* **47**, D607-D613 (2019).
75 Naylor, A. J. *et al.* A differential role for CD248 (Endosialin) in PDGF-mediated skeletal muscle angiogenesis. *PLoS One* **9** (2014).
76 Sun, J. & Nan, G. The mitogen-activated protein kinase (MAPK) signaling pathway as a discovery target in stroke. *Journal of Molecular Neuroscience* **59**, 90-98 (2016).
77 Kanehisa, M., Sato, Y., Furumichi, M., Morishima, K. & Tanabe, M. New approach for understanding genome variations in KEGG. *Nucleic acids research* **47**, D590-D595 (2019).
78 Soofi, S. S., Last, J. A., Liliensiek, S. J., Nealey, P. F. & Murphy, C. J. The elastic modulus of Matrigel™ as determined by atomic force microscopy. *J Struct Biol* **167**, 216-219 (2009).
79 Grant, S. G. Synapse molecular complexity and the plasticity behaviour problem. *Brain and Neuroscience Advances* **2**, 2398212818810685 (2018).
80 Janowski, M., Wagner, D.-C. & Boltze, J. Stem cell–based tissue replacement after stroke: factual necessity or notorious fiction? *Stroke* **46**, 2354-2363 (2015).
81 Ohab, J. J. & Carmichael, S. T. Poststroke neurogenesis: emerging principles of migration and localization of immature neurons. *The Neuroscientist* **14**, 369 (2008).
82 Campisi, M. *et al.* 3D self-organized microvascular model of the human blood-brain barrier with endothelial cells, pericytes and astrocytes. *Biomaterials* **180**, 117-129 (2018).
83 Booth, R. & Kim, H. Characterization of a microfluidic in vitro model of the blood-brain barrier (μBBB). *Lab on a Chip* **12**, 1784-1792 (2012).
84 Sances, S. *et al.* Human iPSC-derived endothelial cells and microengineered organ-chip enhance neuronal development. *Stem cell reports* **10**, 1222-1236 (2018).
85 Vatine, G. D. *et al.* Human iPSC-derived blood-brain barrier chips enable disease modeling and personalized medicine applications. *Cell stem cell* **24**, 995-1005. e1006 (2019).
86 Xu, L., Nirwane, A. & Yao, Y. Basement membrane and blood–brain barrier. *Stroke Vasc. Neurol.* **4**, 78-82 (2019).
87 Eddington, D. T., Puccinelli, J. P. & Beebe, D. J. Thermal aging and reduced hydrophobic recovery of polydimethylsiloxane. *Sensors and Actuators B: Chemical* **114**, 170-172 (2006).
88 Halldorsson, S., Lucumi, E., Gómez-Sjöberg, R. & Fleming, R. M. Advantages and challenges of microfluidic cell culture in polydimethylsiloxane devices. *Biosensors and Bioelectronics* **63**, 218-231 (2015).
89 Ma, X. *et al.* Injection molding and characterization of PMMA-based microfluidic devices. *Microsystem Technologies* **26**, 1317-1324 (2020).
90 Daadi, M. M., Maag, A.-L. & Steinberg, G. K. Adherent self-renewable human embryonic stem cell-derived neural stem cell line: functional engraftment in experimental stroke model. *PloS one* **3**, e1644 (2008).
91 Offner, H., Vandenbark, A. & Hurn, P. D. Effect of experimental stroke on peripheral immunity: CNS ischemia induces profound immunosuppression. *Neuroscience* **158**, 1098-1111 (2009).
92 Ajami, N. E. *et al.* Systems biology analysis of longitudinal functional response of endothelial cells to shear stress. *Proceedings of the National Academy of Sciences* **114**, 10990-10995 (2017).
93 Wang, C., Baker, B. M., Chen, C. S. & Schwartz, M. A. Endothelial cell sensing of flow direction. *Arteriosclerosis, thrombosis, and vascular biology* **33**, 2130-2136 (2013).
94 Rikhtegar, R. *et al.* Stem cell-based cell therapy for neuroprotection in stroke: A review. *Journal of cellular biochemistry* **120**, 8849-8862 (2019).
95 Huertas-Vazquez, A., Leon-Mimila, P. & Wang, J. Relevance of multi-omics studies in cardiovascular diseases. *Frontiers in cardiovascular medicine* **6**, 91 (2019).
96 Mi, S., Du, Z., Xu, Y. & Sun, W. The crossing and integration between microfluidic technology and 3D printing for organ-on-chips. *Journal of Materials Chemistry B* **6**, 6191-6206 (2018).
97 von Bartheld, C. S., Bahney, J. & Herculano-Houzel, S. The search for true numbers of neurons and glial cells in the human brain: A review of 150 years of cell counting. *Journal of Comparative Neurology* **524**, 3865-3895 (2016).
98 Gunhanlar, N. *et al.* A simplified protocol for differentiation of electrophysiologically mature neuronal networks from human induced pluripotent stem cells. *Molecular psychiatry* **23**, 1336-1344 (2018).
99 Dore-Duffy, P. *et al.* Pericyte migration from the vascular wall in response to traumatic brain injury. *Microvascular research* **60**, 55-69 (2000).
100 Luissint, A.-C., Artus, C., Glacial, F., Ganeshamoorthy, K. & Couraud, P.-O. Tight junctions at the blood brain barrier: physiological architecture and disease-associated dysregulation. *Fluids and Barriers of the CNS* **9**, 23 (2012).
101 Vormann, M. K. *et al.* Nephrotoxicity and kidney transport assessment on 3D perfused proximal tubules. *The AAPS journal* **20**, 90 (2018).
102 Yang, L., Shah, K. K. & Abbruscato, T. J. An in vitro model of ischemic stroke. *Astrocytes*, 451-466 (2012).

1060 103 Curry, F., Huxley, V. & Adamson, R. Permeability of single capillaries to intermediate-sized colored solutes.
1061 *American Journal of Physiology-Heart and Circulatory Physiology* **245**, H495-H505 (1983).
1062 104 Haase, K., Gillrie, M. R., Hajal, C. & Kamm, R. D. Pericytes Contribute to Dysfunction in a Human 3D Model of
1063 Placental Microvasculature through VEGF-Ang-Tie2 Signaling. *Advanced Science* **6**, 1900878 (2019).
1064 105 Shin, Y. *et al.* Blood–Brain Barrier Dysfunction in a 3D In Vitro Model of Alzheimer's Disease. *Advanced Science* **6**,
1065 1900962 (2019).
1066 106 Lee, S. W. L. *et al.* Modeling Nanocarrier Transport across a 3D In Vitro Human Blood-Brain–Barrier
1067 Microvasculature. *Advanced Healthcare Materials* **9**, 1901486 (2020).
1068 107 Boussommier-Calleja, A. *et al.* The effects of monocytes on tumor cell extravasation in a 3D vascularized microfluidic
1069 model. *Biomaterials* **198**, 180-193 (2019).
1070 108 Rodríguez-Frutos, B. *et al.* Stem cell therapy and administration routes after stroke. *Translational stroke research* **7**,
1071 378-387 (2016).
1072

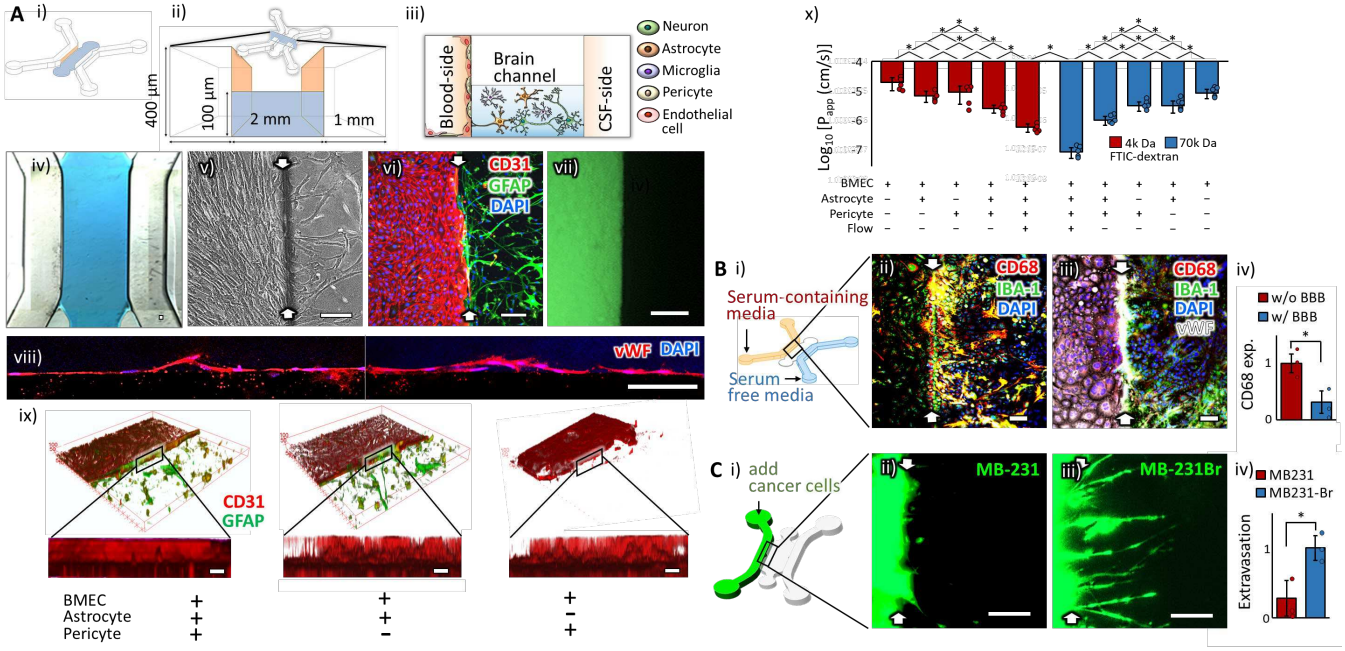

Figure 1. Chip design for functional BBB formation. A. physically intact barrier. (i-ii) The schematic illustration of the chip design w/o micro-poles and **(iii)** the spatial distribution of the NVU constituent cells in the chip. **(iv)** A bright field image showing the hydrogel (blue) deployed in the 'brain' channel. **(v-vi)** The well-defined boundaries (white arrows) between the 'blood-side' and 'brain' channels are shown in a phase contrast (v) and a fluorescence (vi) images. Endothelial cells and astrocytes were stained by CD31 and GFAP, respectively. **(vii)** The formed endothelium prevented free diffusion of the green fluorescent probes (FITC-Dextran, 4k Da) across it. The image was taken one hour after adding the probes. **(viii)** Single layers of confocal microscopic images of the formed endothelium on the side wall of the hydrogel. The endothelial cells were stained by von Willebrand factor (VWF). **(ix)** The 3D reconstructed view of the confocal microscopic images showing the uniform endothelium formation by the interaction with astrocytes and pericytes. Endothelial cells and astrocytes were immunostained with their specific markers, CD31 and GFAP, respectively. **(x)** Log-transformed values of apparent permeability coefficients, P_{app}, of the endothelium in the chips (n=5). **B. Biochemically intact barrier. (i)** The schematic illustration of the hybrid culture condition with serum-containing media in the 'blood-side' channel and serum-free media in the 'CSF-side' channel. **(ii)** In the sample w/o endothelium (white arrows indicated the hydrogel boundary), microglia (stained as green by IBA-1) upregulated the expression of CD68 (red), a pro-inflammatory microglial marker, and appeared as yellow. **(iii)** In the sample with the reconstructed endothelium, most of the microglia did not express CD68. **(iv)** The CD68 expression between the samples w/ and w/o endothelium (n=3). All analyses were made 24 hours after serum was added. **C. Cell-selective barrier. (i)** The schematic illustration showing the cancer cell incorporation. The prestaind cells of two human breast cancer cell lines, MB-231 and MB-231Br, were injected into the 'blood-side' channel. **(ii-iii)** The fluorescent images for MB-231(ii) and MB-231Br (iii), taken 1 day after the injection. White arrows indicate the hydrogel boundary. **(iv)** The extent of the extravasation across the BBB was measured 7 days after the cell injection (n=3). The statistical significance is denoted as '*'. 'n' denotes the number of chips used in each experimental condition. Scale bars: 100 µm.

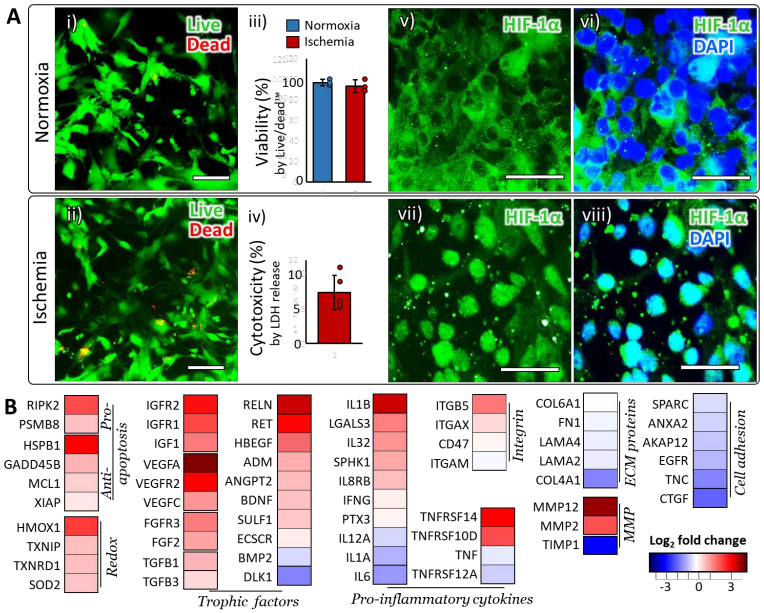

Figure 2. Establishing ischemic condition. A. (i-ii) Live/dead assay: Live cells were stained as green by calcein AM, while dead cells were stained as red by ethidium homodimer (EthD-1). Scale bars: 100 µm. **(iii)** Quantified viability measured by Live/dead assay (n=3). **(iv)** Cytotoxicity measured by extracellular LDH level (n=5). **(v-viii)** In normoxia, HIF-1 α mainly located in the cytoplasm (i-ii). In our ischemic condition, HIF-1α accumulated in the nucleus (iii-iv). All images were taken from the 'brain' channel. **B.** Gene expression alteration induced by ischemia. *Log*$_2$ fold changes are plotted in the heatmap. The genes are clustered into groups according to their functions. More detailed description on the functions of each gene are presented in **Table S2** in S.I.

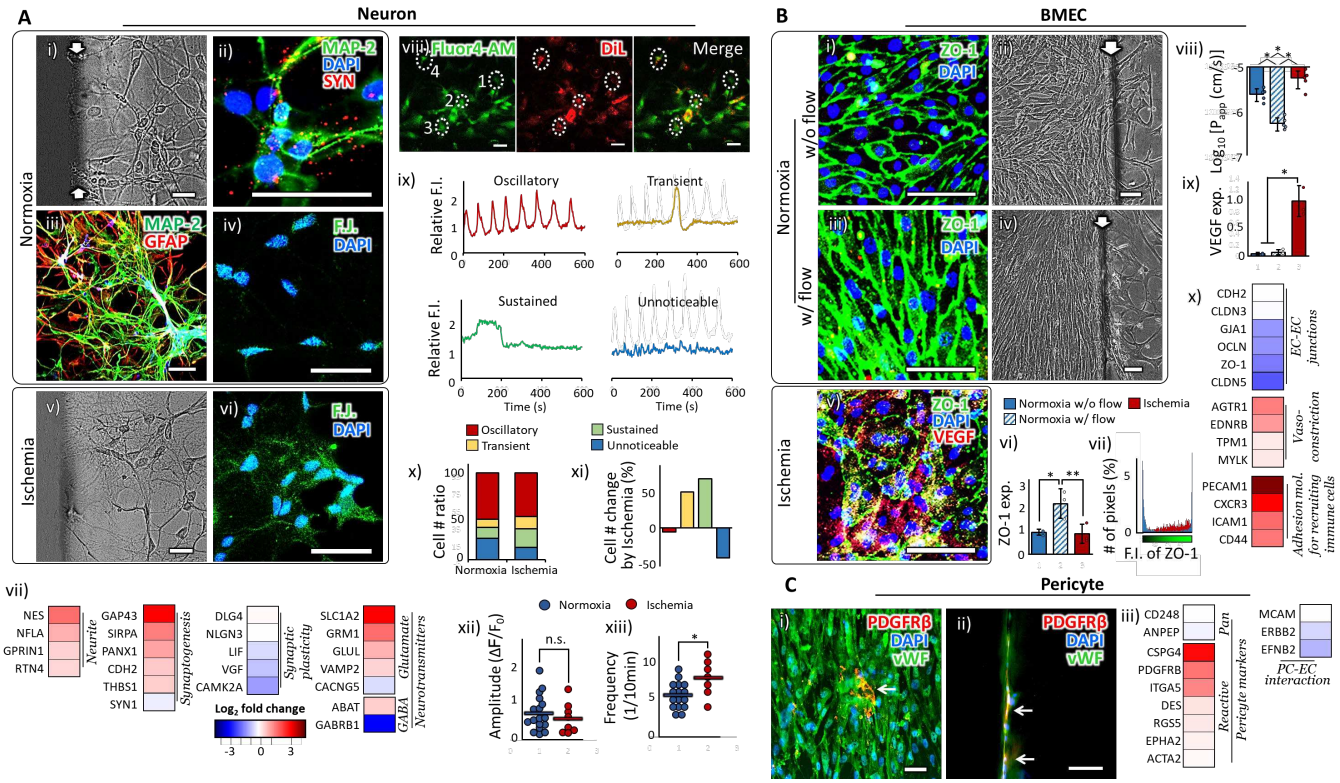

Figure 3. Behaviors of neurons, BMEC and pericytes in our stroke model. A. Neuron. (i) A phase contract image of neurons in a normoxic sample. **(ii)** The neurons derived from human iPSC expressed mature neuronal markers, MAP-2 and Synapsin I and II (SYN). **(iii)** NVU cellular components were immuno-stained with a neuronal marker, MAP-2, and an astrocyte marker, GFAP. **(iv)** Fluoro-Jade C, a neuronal degeneration marker, barely stained the neurons in normoxia. **(v)** A phase contract image of neurons in a hypoxic sample. **(vi)** Fluoro-Jade C stained the neurons in hypoxia. **(vii)** Gene expression alteration by ischemia. **(viii-xiii)** *Spontaneous oscillations of cytosolic calcium ions (Ca^{2+}) in differentiated NPC.* **(viii-ix)** A representative calcium recording image (viii). NPC were prestaiend with DiL (red). Fluo-4 AM (green) was used to detect cytosolic Ca^{2+} concentration. The DiL-expressing cells were randomly chosen from four independent samples, two each in normoxia (34 cells) and ischemia condition (14 cells). The differentiated NPC showed four distinct Ca^{2+} oscillation patterns for 10 minutes of recording (ix). The marked cells from 1 to 4 in (viii) showed oscillatory, transient, sustained and unnoticeable patterns, respectively. **(x-xi)** The ratio of cell numbers for each Ca^{2+} oscillation pattern (x) and the changes in the cell numbers due to ischemia (xi). **(xii-xiii)** The amplitude and frequency of the calcium oscillation in the cells showing oscillatory Ca^{2+} signals. The horizontal bars indicate the mean values. **B. BMEC. (i-iv)** The fluorescent (i vs. iii) and phase contrast (ii vs. iv) images show the BMEC morphology with or without flow. **(v)** The ZO-1 and VEGF expression spread all over the bodies of BMEC in ischemia. **(vi)** The overall extent of ZO-1 expression in BMEC is increased with the introduction of flow and reduced back in ischemic condition (n=3). **(vii)** The spatial distribution of ZO-1 expression in an individual cell is quantified by counting the number of pixels (y-axis) corresponding the fluorescent intensity (x-axis). The ZO-1 expression in the ischemic cells is dispersed throughout the entire cell body in contrast to the pattern of localized peaks shown in normoxic cells. **(viii)** The changes of log-transformed P_{app} by the presence of flow and ischemic insult (n=3). **(ix)** BMEC in ischemia upregulated the VEGF expression (n=3). **(x)** Gene expression alteration by ischemia. **C. Pericyte. (i-ii)** A few pericytes are exposed between BMEC (i) and

1136 on the side wall of the ‘brain’ channel (ii). White arrows indicate pericytes. More detailed data on
1137 pericytes distribution are presented in **Fig. S3**. **(ii)** Gene expression alteration by ischemia. More details
1138 on the functions of each gene are presented in **Table S2** in S.I. Statistical significance is denoted as ‘*’.
1139 White arrows indicate the hydrogel boundary between the ‘blood-side’ and the ‘brain’ channels. ‘n’
1140 denotes the number of chips used in each experimental condition. Scale bars: 50 µm.

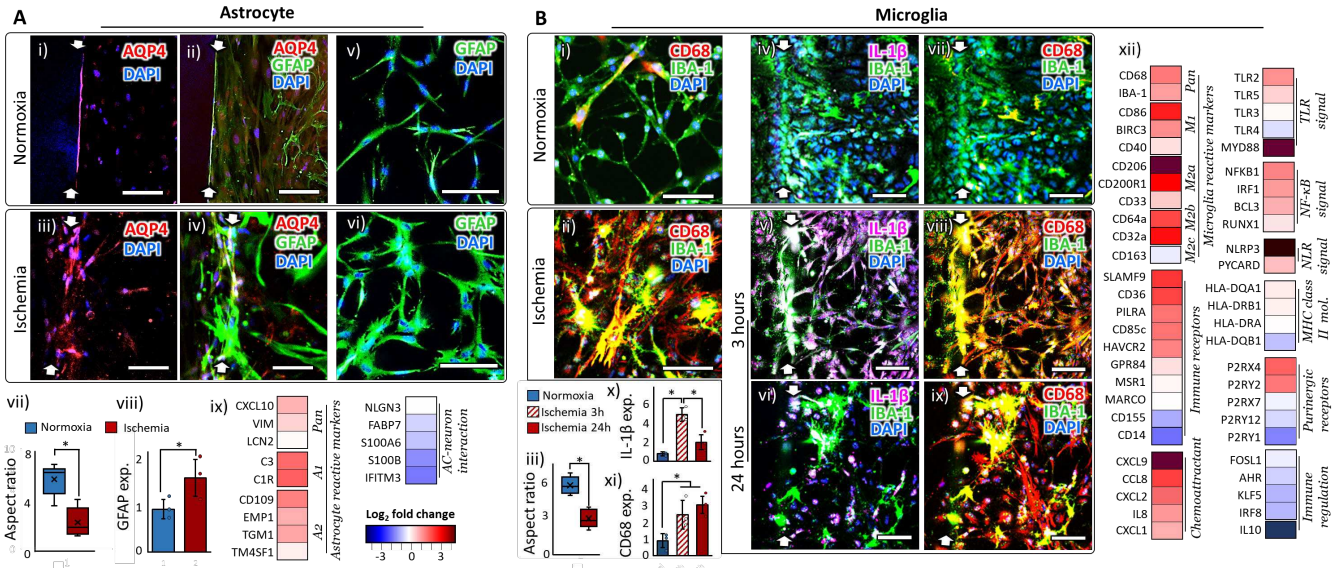

Figure 4. Behaviors of astrocyte and microglia in our stroke model. A. Astrocyte. (i-iv) AQP4 in the normoxic astrocytes are localized along the formed endothelium on the side wall of the hydrogel (i-ii), while AQP4 in the ischemic astrocytes spread over the cell bodies (iii-iv). **(v-viii)** Astrocytes in ischemic condition show hypertrophic morphology (vii, more than 15 cells from 3 chips were analyzed.) and upregulated GFAP expression (viii, n=3). The aspect ratio is calculated by taking the ratio between the longest axis of a cell body and the shortest axis. **(ix)** Gene expression alteration by ischemia. **B. Microglia. (i-ii)** Microglia (stained by IBA-1) in ischemia express CD68. **(iii)** Microglia in ischemia round out their cell body compared to normoxic microglia. More than 15 cells from 3 chips were analyzed. **(iv-xi)** Microglia upregulate the expression of IL-1β only during the first a few hours of the ischemic onset (x, n=3). CD68 is expressed in microglia for the whole duration of the ischemic condition (xi, n=3). **(xii)** Gene expression alteration by ischemia. More details on the functions of each gene are presented in **Table S2** in S.I. White arrows indicate the hydrogel boundary between the 'blood-side' and the 'brain' channels. 'n' denotes the number of chips used in each experimental condition. Statistical significance is denoted as '*'. Scale bars: 50 μm.

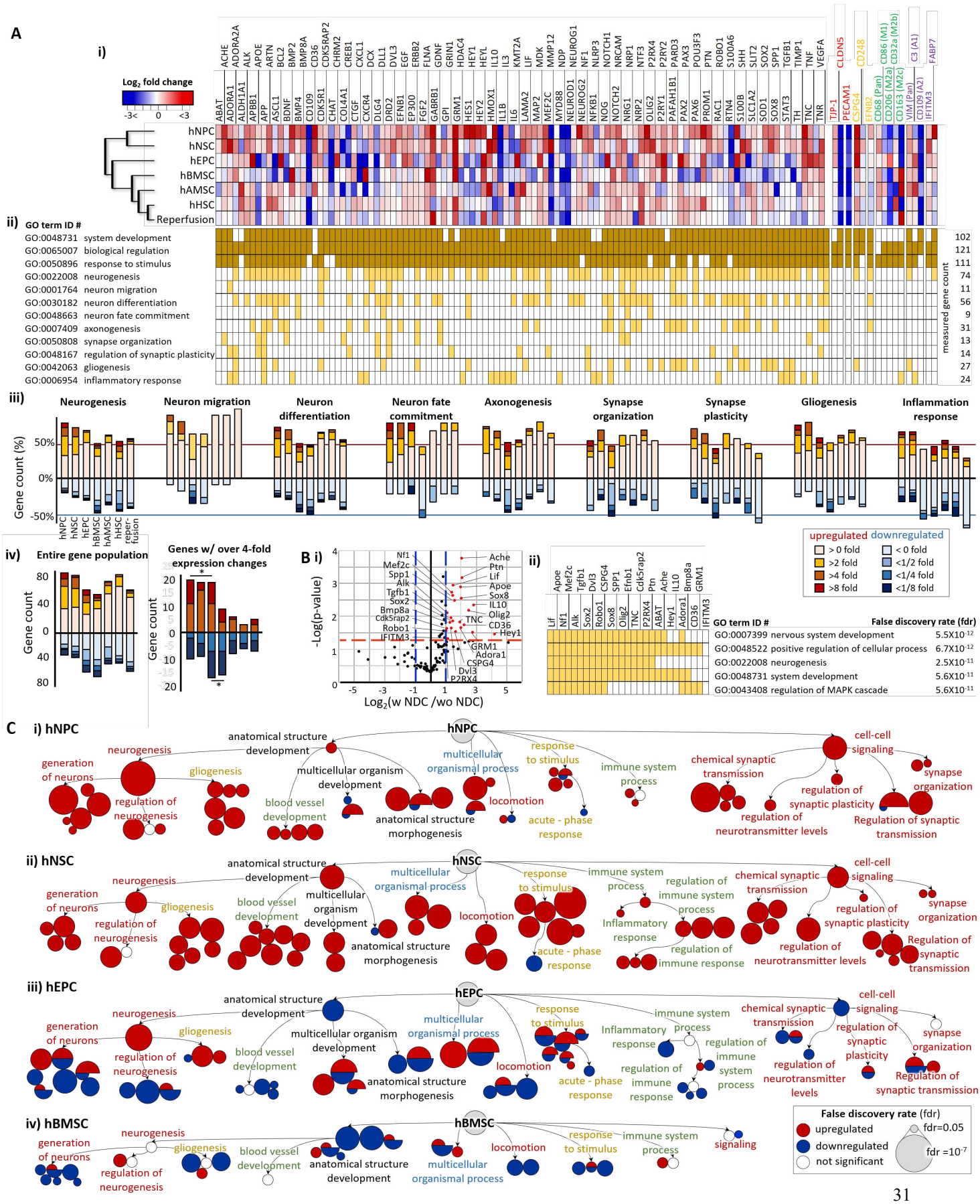
A
i)
Log2 fold change
-3<
0
<3
hNPC
hNSC
hEPC
hBMSC
hAMSC
hHSC
Reperfusion
ii)
GO term ID #
GO:0048731 system development
GO:0065007 biological regulation
GO:0050896 response to stimulus
GO:0022008 neurogenesis
GO:0001764 neuron migration
GO:0030182 neuron differentiation
GO:0048663 neuron fate commitment
GO:0007409 axonogenesis
GO:0050808 synapse organization
GO:0048167 regulation of synaptic plasticity
GO:0042063 gliogenesis
GO:0006954 inflammatory response
measured gene count
102
121
111
74
11
56
9
31
13
14
27
24
iii)
Neurogenesis
Neuron migration
Neuron differentiation
Neuron fate commitment
Axonogenesis
Synapse organization
Synapse plasticity
Gliogenesis
Inflammation response
Gene count (%)
50%
0%
-50%
hNPC
hNSC
hEPC
hBMSC
hAMSC
hHSC
reper-fusion
iv)
Entire gene population
Genes w/ over 4-fold expression changes
Gene count
upregulated
downregulated
> 0 fold
>2 fold
>4 fold
>8 fold
< 0 fold
<1/2 fold
<1/4 fold
<1/8 fold
B i)
-Log(p-value)
Log2(w NDC /wo NDC)
Nf1
Mef2c
Spp1
Alk
Tgfb1
Sox2
Bmp8a
Cdk5rap2
Robo1
IFITM3
Ache
Ptn
Lif
Apoe
Sox8
IL10
Olig2
CD36
Hey1
TNC
GRM1
Adora1
CSPG4
Dvl3
P2RX4
ii)
GO term ID #
False discovery rate (fdr)
GO:0007399 nervous system development 5.5X10-12
GO:0048522 positive regulation of cellular process 6.7X10-12
GO:0022008 neurogenesis 2.5X10-11
GO:0048731 system development 5.6X10-11
GO:0043408 regulation of MAPK cascade 5.6X10-11
C
i) hNPC
ii) hNSC
iii) hEPC
iv) hBMSC
hNPC
hNSC
hEPC
hBMSC
generation of neurons
neurogenesis
gliogenesis
regulation of neurogenesis
anatomical structure development
multicellular organism development
blood vessel development
anatomical structure morphogenesis
multicellular organismal process
response to stimulus
immune system process
locomotion
acute - phase response
chemical synaptic transmission
cell-cell signaling
synapse organization
regulation of synaptic plasticity
regulation of neurotransmitter levels
Regulation of synaptic transmission
Inflammatory response
regulation of immune system process
regulation of immune response
signaling
False discovery rate (fdr)
upregulated
downregulated
not significant
fdr=0.05
fdr =10-7

1159 **Figure 5. Characterization of the neurorestorative potential of stem cells. A. (i)** A heat map for the gene
1160 expression alteration 7 days after incorporating stem cells in ischemic samples. More detailed functions
1161 of each gene are described in **Table S2** & **S3**. The gene names written in red, yellow, green and purple are
1162 the phenotype markers of endothelial cells, pericytes, microglia and astrocytes, respectively. **(ii)** GO
1163 terms associated each gene are highlighted in yellow. **(iii)** The graphs show the percentage of genes
1164 associated with each GO term according to their expression fold changes (Increase for red and decrease
1165 for blue). **(iv)** The graphs show the gene count of the entire population of genes according to their
1166 expression fold changes. The genes with over 4-fold expression changes are shown in the right. Statistical
1167 significance in the up/down regulated gene counts is denoted as '*'. **B. (i)** The graph identifies the genes
1168 (red) expressed differentially by the stem cell types with the neuronal differentiation capacity (NDC). The
1169 cut-off thresholds are the p-value of 0.05 (red dash line) and more than 2-fold expression changes (blue
1170 dash line). **(ii)** The five most significant GO terms emerged from the GO enrichment analysis of the genes
1171 identified in (i). GO terms associated with each gene are highlighted in yellow. **C.** The GO term enrichment
1172 networks, built only with the genes with more than 4-fold expression changes, show the dominant
1173 restorative pathways for each stem cell type. The clustered circles around the GO-term labeled circle
1174 indicate its significant subtrees in GO hierarchy. The detailed GO terms are shown in **Figure S10**.

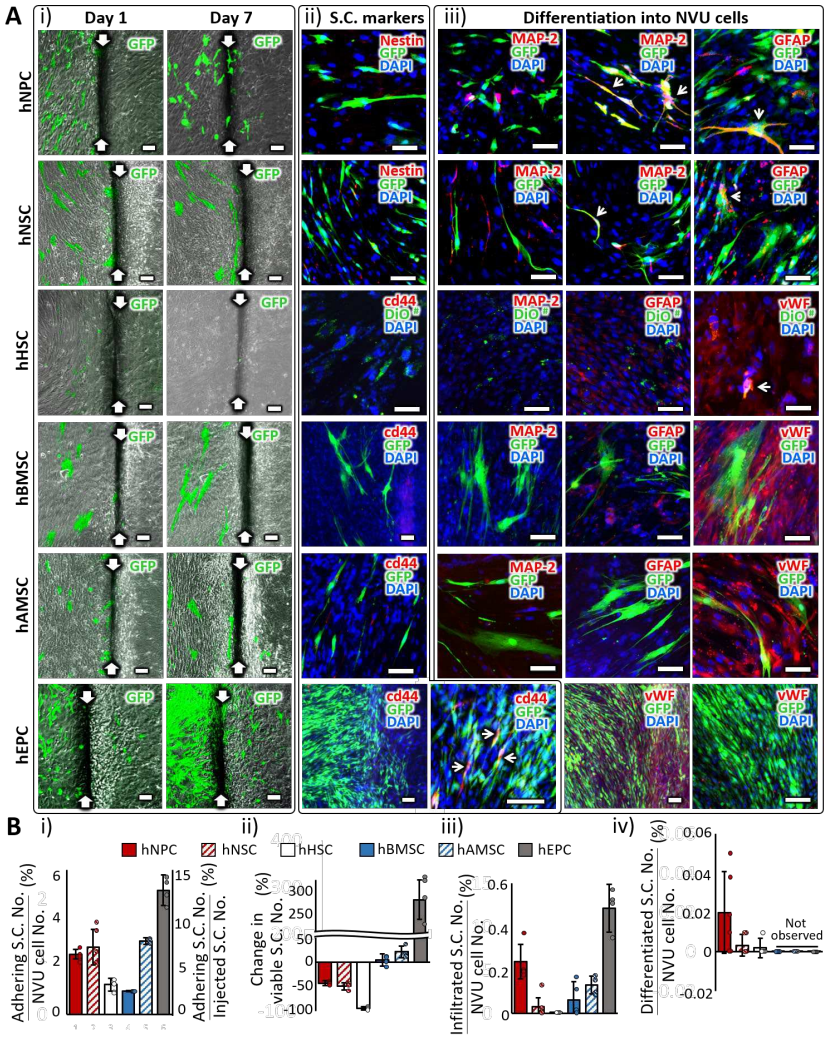

Figure 6. Tracking of the transplanted stem cells. A. (i) Images of GFP-expressing stem cells in 1 day and 7 days after transplantation. White arrows indicate the hydrogel boundary. **(ii)** Expression of stem cell (S.C.) markers 7 days after transplantation. Cells co-expressing GFP and S.C. marker are indicated with white arrows. The cells expressing S.C. markers were selectively chosen for imaging since they were very scarce. **(iii)** Expression of lineage markers (MAP-2: Neuron, GFAP: Astrocyte and vWF: endothelial cell) that each S.C. type could differentiate into. Cells co-expressing GFP and lineage marker are indicated with white arrows. The cells expressing differentiation markers were selectively chosen for imaging. # Due to the limited number of GFP-expressing hHSC, we incorporated pre-stained cells with a cell membrane-labeling dye, DiO. Scale bars: 100 µm. **B. (i)** The percentage of the stem cell numbers adhering on the chip with respect to the total cell number (vertical axis on the left) and with respect to the number of injected stem cells (vertical axis on the right) in the chip. Measured one day after injection. **(ii)** The changes in the viable S.C. numbers compared between 1 day and 7 days after transplantation. **(iii)** The percentage of the stem cell numbers infiltrated across the BBB with respect to the total cell number in the chip. Measured 7 days after injection. **(iv)** The percentage of the stem cell numbers differentiated into the NVU constituent cell types with respect to the total cell number in the chip. Measured 7 days after injection. The NVU cell number in the chip was assumed to stay throughout the incubation period. More than 3 images were obtained from 3 chips for each experimental condition.

1193 **Supplementary Information (S.I.)**

1194 **Table S1**. Workflow for the sample preparation
1195 **Fig. S1**. Endothelium defects in a chip with micro-poles
1196 **Fig. S2**. Master mold images of the chips.
1197 **Fig. S3**. Spatial cell distribution in the chip
1198 **Fig. S4**. Morphological changes of BMEC due to the interaction with glial cells
1199 **Fig. S5**. TEER values of the BBB.
1200 **Fig. S6**. Expression changes of BBB markers by flow
1201 **Fig. S7**. Astrocyte behaviors in 2D culture
1202 **Fig. S8**. Microglia behavior in 2D culture
1203 **Fig. S9**. Gene expression alteration of glia phenotype markers by transplanted stem cells and
1204 reperfusion
1205 **Fig. S10**. GO terms from the functional enrichment analysis on the genes with over 4-fold
1206 expression changes
1207 **Fig. S11**. GO terms from the functional enrichment analysis on the genes with over 2-fold
1208 expression changes
1209 **Fig. S12**. GO terms related to synapse and neurotransmitters, from the functional enrichment
1210 analysis on the genes with over both 4- and 2-fold expression changes
1211 **Fig. S13**. GFP transfection efficiency
1212 **Fig. S14**. Time-lapse images of GFP-expressing stem cells invading across the BBB on a chip
1213 **Fig. S15**. Fluorescent images showing the expression of stem cell markers in 2D culture before
1214 the transplantation
1215 **Table S2**. Functional characteristics and relevant references of the genes in **Figure 2**, **3**, and **4**.
1216 **Table S3**. Functional characteristics and relevant references of the genes in **Figure 5**.
1217 **References** for the gene information

Figures

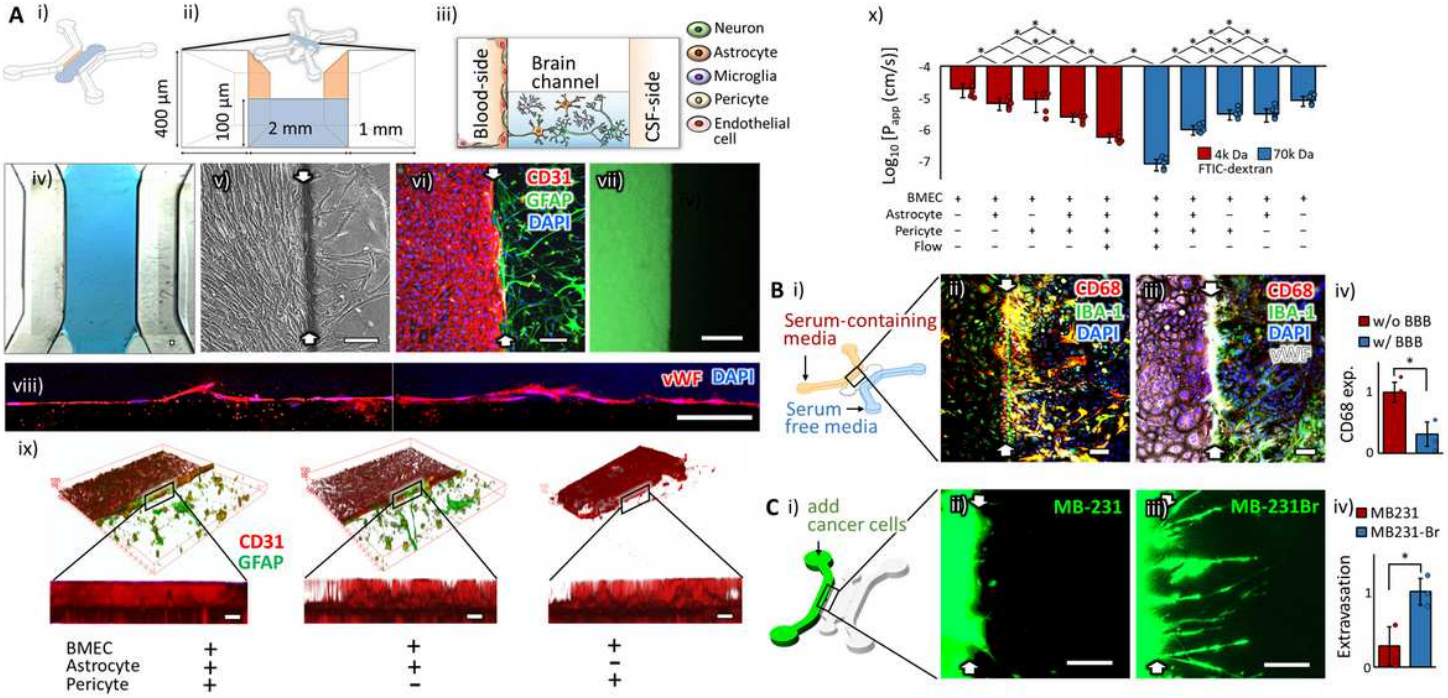

Figure 1

Chip design for functional BBB formation. A. physically intact barrier. (i-ii) The schematic illustration of the chip design w/o micro-poles and (iii) the spatial distribution of the NVU constituent cells in the chip. (iv) A bright field image showing the hydrogel (blue) deployed in the 'brain' channel. (v-vi) The well-defined boundaries (white arrows) between the 'blood-side' and 'brain' channels are shown in a phase contrast (v) and a fluorescence (vi) images. Endothelial cells and astrocytes were stained by CD31 and GFAP, respectively. (vii) The formed endothelium prevented free diffusion of the green fluorescent probes (FITC-Dextran, 4k Da) across it. The image was taken one hour after adding the probes. (viii) Single layers of confocal microscopic images of the formed endothelium on the side wall of the hydrogel. The endothelial cells were stained by von Willebrand factor (VWF). (ix) The 3D reconstructed view of the confocal microscopic images showing the uniform endothelium formation by the interaction with astrocytes and pericytes. Endothelial cells and astrocytes were immunostained with their specific markers, CD31 and GFAP, respectively. (x) Log-transformed values of apparent permeability coefficients, Papp, of the endothelium in the chips (n=5). B. Biochemically intact barrier. (i) The schematic illustration of the hybrid culture condition with serum-containing media in the 'blood-side' channel and serum-free media in the 'CSF-side' channel. (ii) In the sample w/o endothelium (white arrows indicated the hydrogel boundary), microglia (stained as green by IBA-1) upregulated the expression of CD68 (red), a pro-inflammatory microglial marker, and appeared as yellow. (iii) In the sample with the reconstructed endothelium, most of the microglia did not express CD68. (iv) The CD68 expression between the samples w/ and w/o endothelium (n=3). All analyses were made 24 hours after serum was added. C. Cell-selective barrier. (i) The schematic illustration showing the cancer cell incorporation. The prestaind cells of two human breast

cancer cell lines, MB-231 and MB-231Br, were injected into the 'blood-side' channel. (ii-iii) The fluorescent images for MB-231(ii) and MB-231Br (iii), taken 1 day after the injection. White arrows indicate the hydrogel boundary. (iv) The extent of the extravasation across the BBB was measured 7 days after the cell injection (n=3). The statistical significance is denoted as '*'. 'n' denotes the number of chips used in each experimental condition. Scale bars: 100 μm.

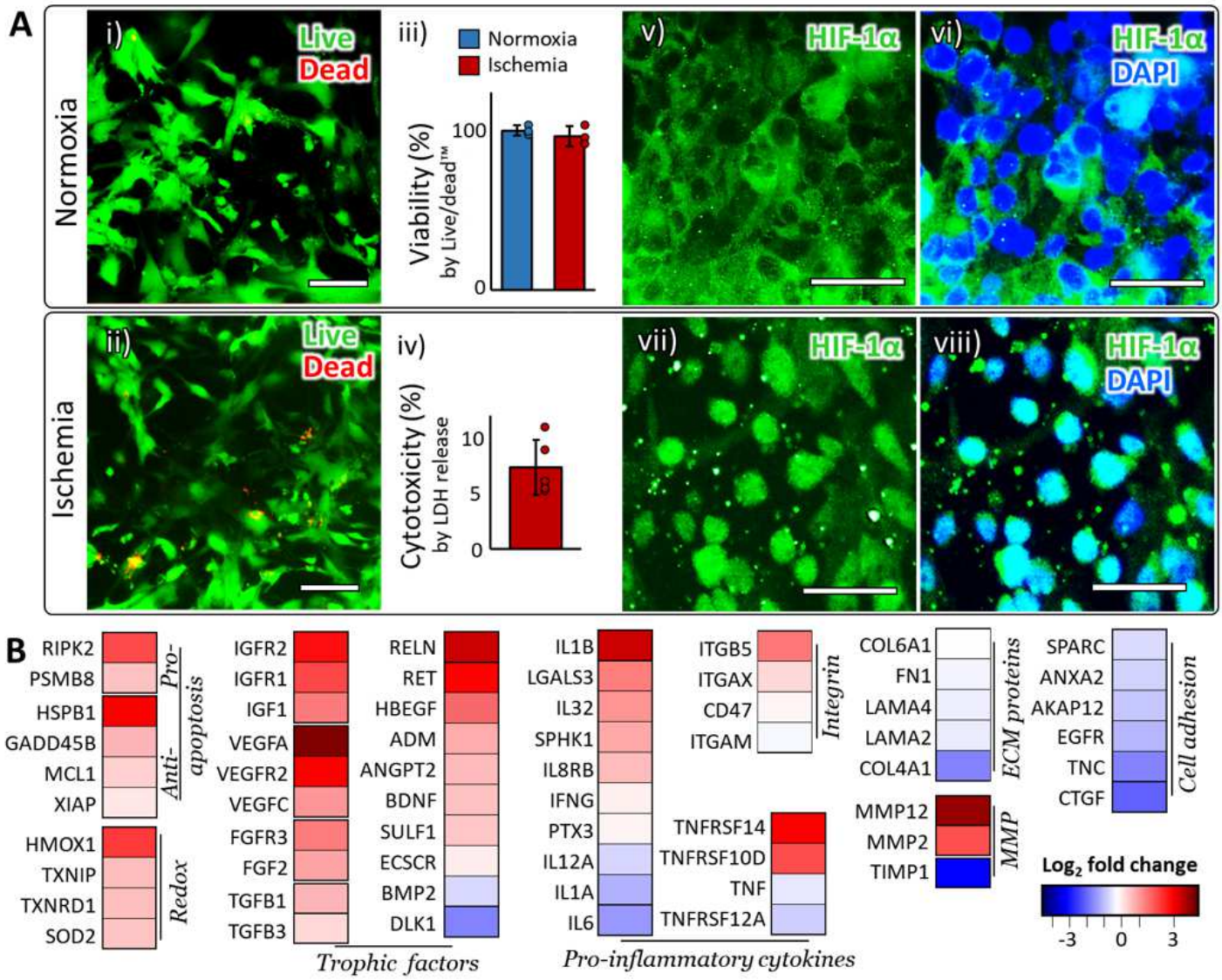

Figure 2

Establishing ischemic condition. A. (i-ii) Live/dead assay: Live cells were stained as green by calcein AM, while dead cells were stained as red by ethidium homodimer (EthD-1). Scale bars: 100 μm. (iii) Quantified viability measured by Live/dead assay (n=3). (iv) Cytotoxicity measured by extracellular LDH level (n=5). (v-viii) In normoxia, HIF-1 α mainly located in the cytoplasm (i-ii). In our ischemic condition, HIF-1α accumulated in the nucleus (iii-iv). All images were taken from the 'brain' channel. B. Gene expression alteration induced by ischemia. Log2 fold changes are plotted in the heatmap. The genes are clustered into groups according to their functions. More detailed description on the functions of each gene are presented in Table S2 in S.I.

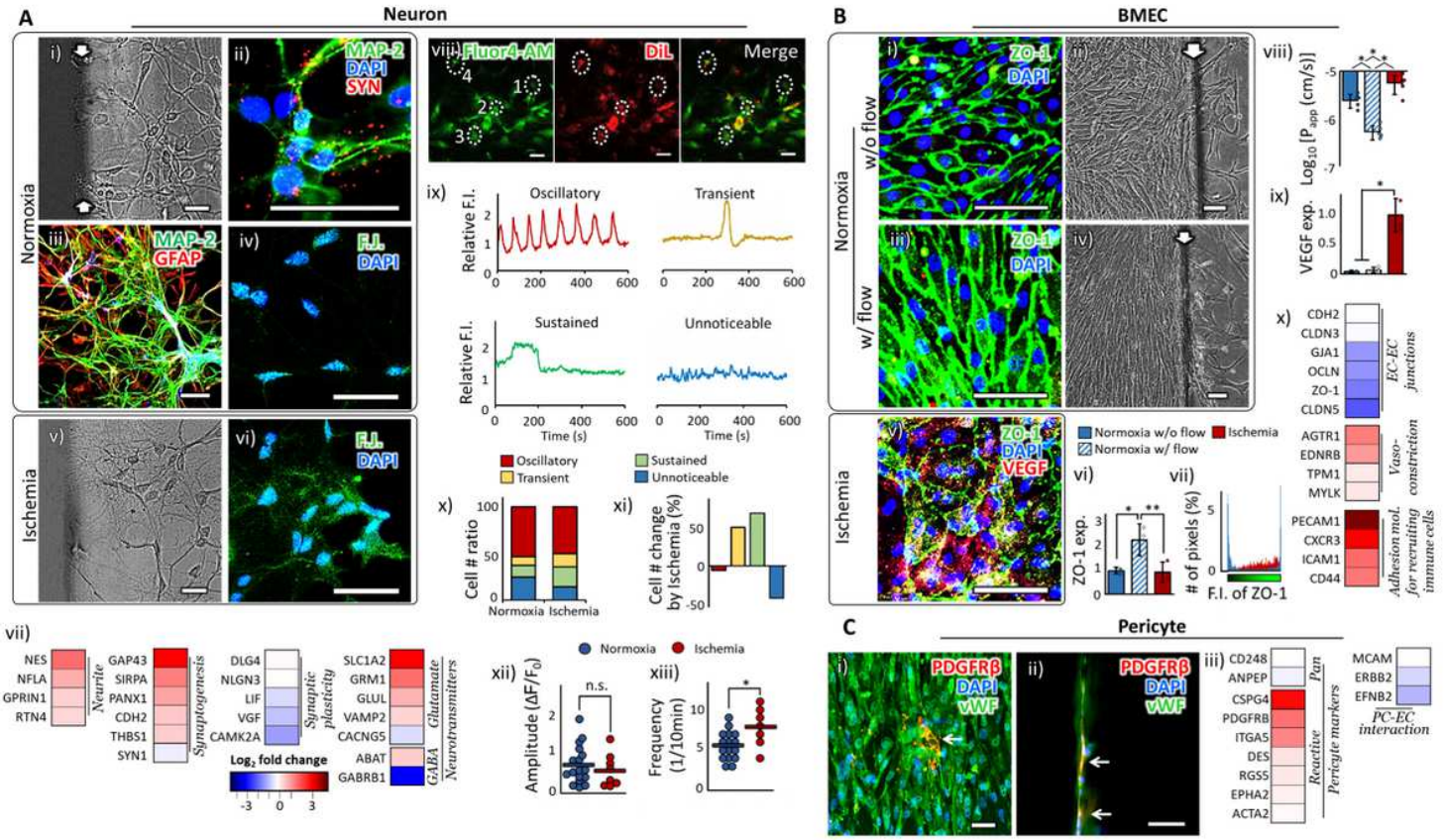

Figure 3

Behaviors of neurons, BMEC and pericytes in our stroke model. A. Neuron. (i) A phase contract image of neurons in a normoxic sample. (ii) The neurons derived from human iPSC expressed mature neuronal markers, MAP-2 and Synapsin I and II (SYN). (iii) NVU cellular components were immuno-stained with a neuronal marker, MAP-2, and an astrocyte marker, GFAP. (iv) Fluoro-Jade C, a neuronal degeneration marker, barely stained the neurons in normoxia. (v) A phase contract image of neurons in a hypoxic sample. (vi) Fluoro-Jade C stained the neurons in hypoxia. (vii) Gene expression alteration by ischemia. (viii-xiii) Spontaneous oscillations of cytosolic calcium ions (Ca2+) in differentiated NPC. (viii-ix) A representative calcium recording image (viii). NPC were prestaiend with DiL (red). Fluo-4 AM (green) was used to detect cytosolic Ca2+ concentration. The DiL-expressing cells were randomly chosen from four independent samples, two each in normoxia (34 cells) and ischemia condition (14 cells). The differentiated NPC showed four distinct Ca2+ oscillation patterns for 10 minutes of recording (ix). The marked cells from 1 to 4 in (viii) showed oscillatory, transient, sustained and unnoticeable patterns, respectively. (x-xi) The ratio of cell numbers for each Ca2+ oscillation pattern (x) and the changes in the cell numbers due to ischemia (xi). (xii-xiii) The amplitude and frequency of the calcium oscillation in the cells showing oscillatory Ca2+ signals. The horizontal bars indicate the mean values. B. BMEC. (i-iv) The fluorescent (i vs. iii) and phase contrast (ii vs. iv) images show the BMEC morphology with or without flow. (v) The ZO-1 and VEGF expression spread all over the bodies of BMEC in ischemia. (vi) The overall extent of ZO-1 expression in BMEC is increased with the introduction of flow and reduced back in ischemic condition (n=3). (vii) The spatial distribution of ZO-1 expression in an individual cell is

quantified by counting the number of pixels (y-axis) corresponding the fluorescent intensity (x-axis). The ZO-1 expression in the ischemic cells is dispersed throughout the entire cell body in contrast to the pattern of localized peaks shown in normoxic cells. (viii) The changes of log-transformed Papp by the presence of flow and ischemic insult (n=3). (ix) BMEC in ischemia upregulated the VEGF expression (n=3). (x) Gene expression alteration by ischemia. C. Pericyte. (i-ii) A few pericytes are exposed between BMEC (i) and on the side wall of the 'brain' channel (ii). White arrows indicate pericytes. More detailed data on pericytes distribution are presented in Fig. S3. (ii) Gene expression alteration by ischemia. More details on the functions of each gene are presented in Table S2 in S.I. Statistical significance is denoted as '*'. White arrows indicate the hydrogel boundary between the 'blood-side' and the 'brain' channels. 'n' denotes the number of chips used in each experimental condition. Scale bars: 50 μm.

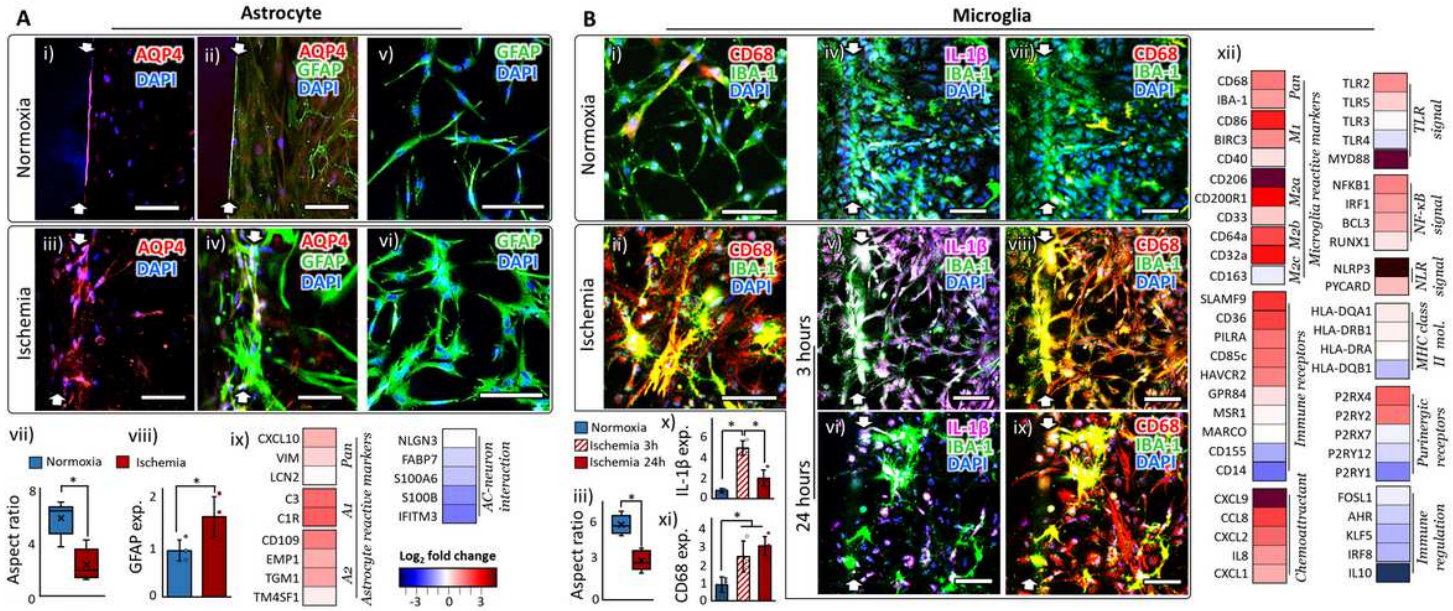

Figure 4

Behaviors of astrocyte and microglia in our stroke model. A. Astrocyte. (i-iv) AQP4 in the normoxic astrocytes are localized along the formed endothelium on the side wall of the hydrogel (i-ii), while AQP4 in the ischemic astrocytes spread over the cell bodies (iii-iv). (v-viii) Astrocytes in ischemic condition show hypertrophic morphology (vii, more than 15 cells from 3 chips were analyzed.) and upregulated GFAP expression (viii, n=3). The aspect ratio is calculated by taking the ratio between the longest axis of a cell body and the shortest axis. (ix) Gene expression alteration by ischemia. B. Microglia. (i-ii) Microglia (stained by IBA-1) in ischemia express CD68. (iii) Microglia in ischemia round out their cell body compared to normoxic microglia. More than 15 cells from 3 chips were analyzed. (iv-xi) Microglia upregulate the expression of IL-1β only during the first a few hours of the ischemic onset (x, n=3). CD68 is expressed in microglia for the whole duration of the ischemic condition (xi, n=3). (xii) Gene expression alteration by ischemia. More details on the functions of each gene are presented in Table S2 in S.I. White arrows indicate the hydrogel boundary between the 'blood-side' and the 'brain' channels. 'n' denotes the number of chips used in each experimental condition. Statistical significance is denoted as '*'. Scale bars: 50 μm.

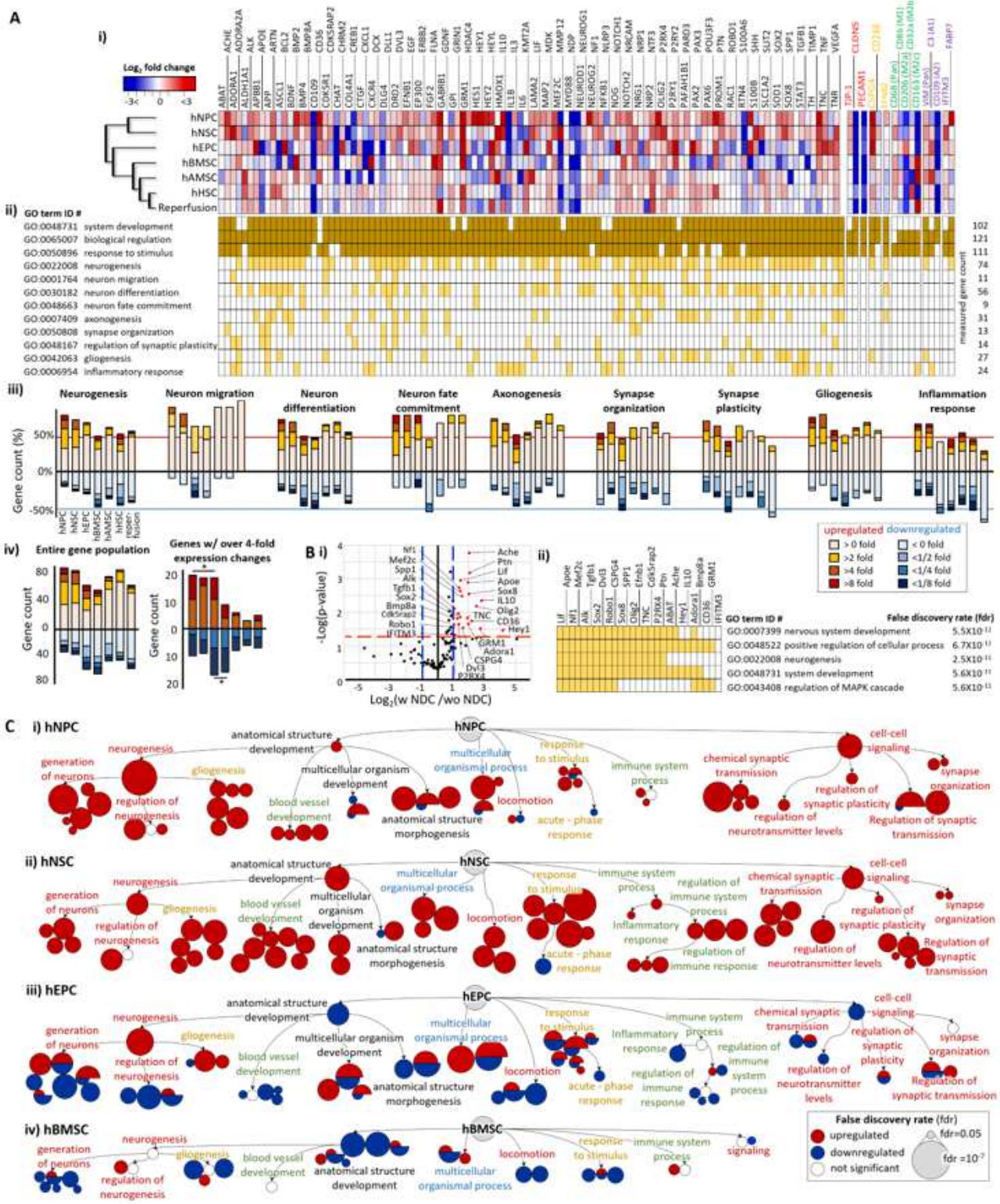

Figure 5

Characterization of the neurorestorative potential of stem cells. A. (i) A heat map for the gene expression alteration 7 days after incorporating stem cells in ischemic samples. More detailed functions of each gene are described in Table S2 & S3. The gene names written in red, yellow, green and purple are the phenotype markers of endothelial cells, pericytes, microglia and astrocytes, respectively. (ii) GO terms associated each gene are highlighted in yellow. (iii) The graphs show the percentage of genes associated

with each GO term according to their expression fold changes (Increase for red and decrease for blue). (iv) The graphs show the gene count of the entire population of genes according to their expression fold changes. The genes with over 4-fold expression changes are shown in the right. Statistical significance in the up/down regulated gene counts is denoted as '*'. B. (i) The graph identifies the genes (red) expressed differentially by the stem cell types with the neuronal differentiation capacity (NDC). The cut-off thresholds are the p-value of 0.05 (red dash line) and more than 2-fold expression changes (blue dash line). (ii) The five most significant GO terms emerged from the GO enrichment analysis of the genes identified in (i). GO terms associated with each gene are highlighted in yellow. C. The GO term enrichment networks, built only with the genes with more than 4-fold expression changes, show the dominant restorative pathways for each stem cell type. The clustered circles around the GO-term labeled circle indicate its significant subtrees in GO hierarchy. The detailed GO terms are shown in Figure S10.

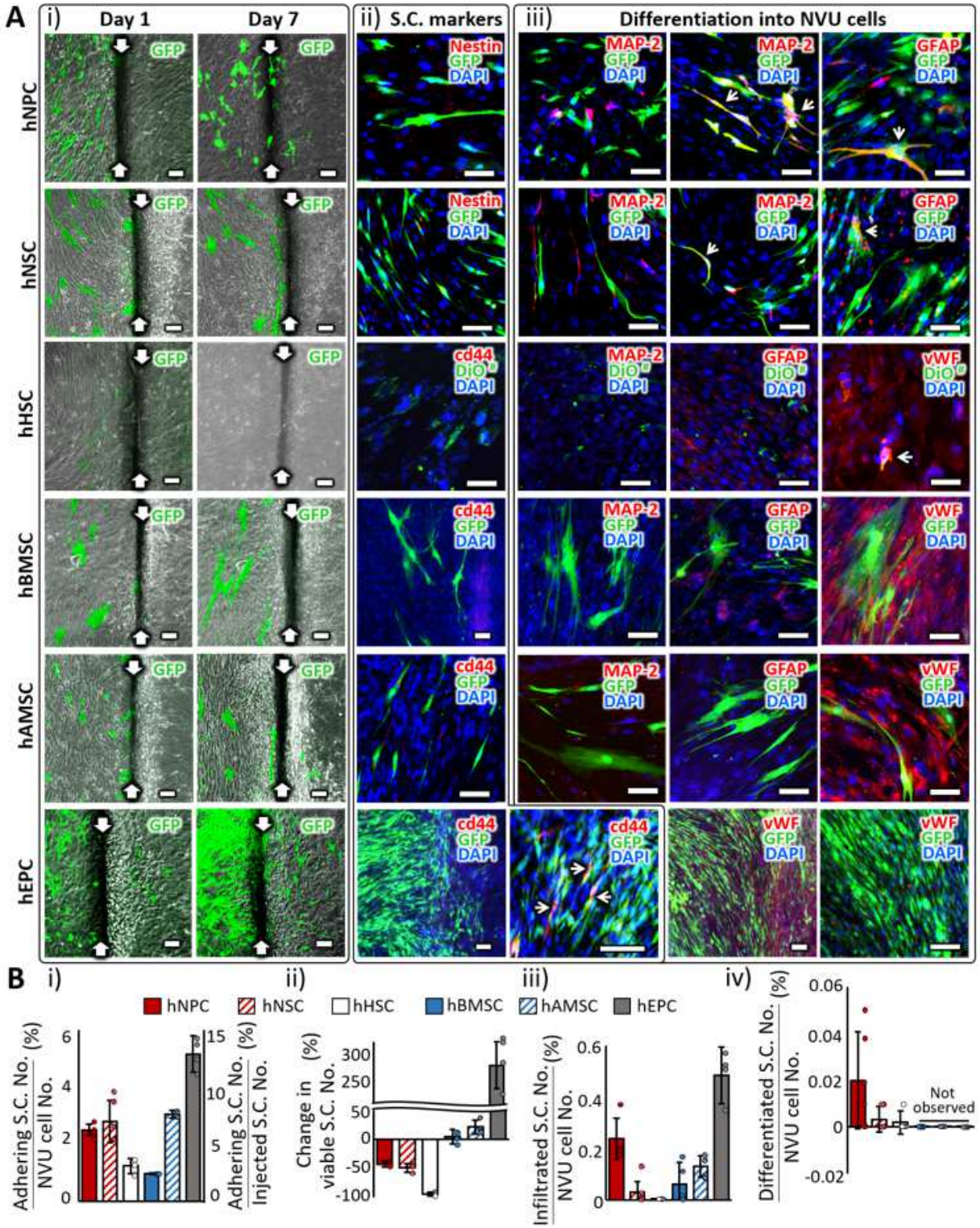

Figure 6

Tracking of the transplanted stem cells. A. (i) Images of GFP-expressing stem cells in 1 day and 7 days after transplantation. White arrows indicate the hydrogel boundary. (ii) Expression of stem cell (S.C.) markers 7 days after transplantation. Cells co-expressing GFP and S.C. marker are indicated with white arrows. The cells expressing S.C. markers were selectively chosen for imaging since they were very scarce. (iii) Expression of lineage markers (MAP-2: Neuron, GFAP: Astrocyte and vWF: endothelial cell)

that each S.C. type could differentiate into. Cells co-expressing GFP and lineage marker are indicated with white arrows. The cells expressing differentiation markers were selectively chosen for imaging. # Due to the limited number of GFP-expressing hHSC, we incorporated pre-stained cells with a cell membrane-labeling dye, DiO. Scale bars: 100 μm. B. (i) The percentage of the stem cell numbers adhering on the chip with respect to the total cell number (vertical axis on the left) and with respect to the number of injected stem cells (vertical axis on the right) in the chip. Measured one day after injection. (ii) The changes in the viable S.C. numbers compared between 1 day and 7 days after transplantation. (iii) The percentage of the stem cell numbers infiltrated across the BBB with respect to the total cell number in the chip. Measured 7 days after injection. (iv) The percentage of the stem cell numbers differentiated into the NVU constituent cell types with respect to the total cell number in the chip. Measured 7 days after injection. The NVU cell number in the chip was assumed to stay throughout the incubation period. More than 3 images were obtained from 3 chips for each experimental condition.

Supplementary Files

This is a list of supplementary files associated with this preprint. Click to download.

- SIStrokechipNBME4thv1.pdf